RSC Advances

Check for updates

Computational modeling and photovoltaic performance evaluation of various ETL/HTL engineered CsCdI₃-based perovskite solar cell architectures

Ashraful Mujahid, [iD] [a] Mohammad Yasin Hayat Khan, [iD] [a] Md Mayen Uddin, [iD] [b] Fahad Alhashmi Alamer, [c] O. Alsalmi, [c] Md. Rasheduzzaman[a] and Md. Zahid Hasan [iD] *[a]

Perovskite solar cells (PSCs) have attracted significant attention in the field of photovoltaic technology owing to their exceptional properties. Despite their high efficiency, the commercial viability of lead-based PSCs is hampered by toxicity. All-inorganic PSCs, particularly those using CsCdI₃ (Cesium Cadmium Triiodide), are promising alternatives. In this study, CsCdI₃-based PSCs were investigated by optimizing various device components. We first investigated nine different back metal contacts (BMCs), and Ni (Nickel) was chosen as the BMC. Following BMC optimization, we assessed the effect of different electron transport layers (ETLs) and hole transport layers (HTLs). Eight distinct HTLs were combined with six ETLs to create unique structures. These configurations were optimized using SCAPS-1D simulation software, with successive enhancements to the thickness and defect density of the absorber and ETL thickness. The optimized structure (ITO/ZnO/CsCdI₃/MoS₂/Ni) achieved exceptional performance: 25.06% power conversion efficiency (PCE), 0.936 V open-circuit voltage (V_{OC}), 30.7 mA cm⁻² short-circuit current density (J_{SC}), and 87.14% fill factor (FF). Furthermore, the dependence on several factors such as (R_s), (R_{sh}), and temperature changes, recombination, generation rates, band alignment (VBO/CBO), J–V characteristics, quantum efficiency (QE), capacitance, and Mott–Schottky (MS) analysis was explored for the six most promising devices. By using tolerance factor analysis, which includes Goldschmidt's and a newly proposed parameter, the structural stability of CsCdI₃ is verified. This research represents significant progress toward an efficient, lead-free, and cost-effective solar cell technology.

1. Introduction

A move toward efficient and sustainable power sources is required owing to the rising energy demand worldwide. Reliance on fossil fuels not only depletes natural reserves but also accelerates environmental degradation and climate change. As these resources diminish, the search for alternative energy solutions becomes crucial. Renewable energy, particularly solar power, offers a promising path forward due to its abundance and minimal environmental impact. Advancements in solar technology continue to improve efficiency and affordability, making it a viable solution to meet future energy needs while reducing dependence on conventional energy sources.

[a]Materials Research and Simulation Lab, Department of Electrical and Electronic Engineering, International Islamic University Chittagong, Kumira, Chittagong, 4318, Bangladesh. E-mail: zahidhasan.02@gmail.com

[b]Department of Electrical, Electronic and Computer Engineering, University of Ulsan, 93 Daehak-ro, Nam-gu, Ulsan 680-749, South Korea

[c]Department of Physics, College of Science, Umm Al-Qura University, Makkah 21955, Saudi Arabia

In recent years, there has been a tremendous growth in electricity consumption, with fossil fuels accounting for a substantial share. Unfortunately, the dependence on fossil fuels adversely affects the ecosystem and contributes to the greenhouse effect.[1–3] Numerous studies are currently being conducted to investigate ecologically beneficial alternative energy sources. Solar cells are becoming the most common and inexpensive solution.[4] To maximize their potential, the development of innovative materials and technologies, such as SCs is crucial.[5] Materials used in photovoltaic cells use the photoelectric effect to transform light particles, or photons, into electrons. Thus, a range of materials, such as organic dyes, semiconductor polymers, metallic oxides like silicon, and other chemical structures with light-absorbing qualities, have been the focus of research on light-absorbing materials appropriate for photovoltaic applications. Metal halide perovskites have drawn interest because of their high carrier mobility, long diffusion length, low excitonic energy, excellent charge mobility, and small band gap. Perovskite solar cells are the most recent in a long line of solar cell generations supported by materials like these.[6]

Organic–inorganic perovskite materials have recently been the subject of intense investigation as a possible replacement for solar cells made of silicon to increase device efficiency.[7,8] This is because they are less expensive to produce.[9] Thin film solar cells (TFSCs), one of the several varieties of PV solar cells, have drawn a lot of attention because of their rapid development and high-performance potential.[10,11] However, the selection of semiconductor growth processes and materials has a significant impact on TFSC efficiency. Although efficiency has increased gradually since the first contemporary silicon solar cell was created in 1954, substantial progress has been achieved, using modules that, by 2010, may generate power from up to 18% of solar radiation.[12] TFSCs—specifically, organic–inorganic metal halide perovskite solar cells—have gained much attention recently because of their exceptional optoelectronic qualities, which include enhanced absorption coefficients, adjustable band gaps, longer electron and hole diffusion lengths, cost-effectiveness, effective charge separation, and solution for solution processing.[13,14] In particular, for next-generation optoelectronic applications including solar cells, light-emitting diodes, transistors, and lasers, organic–inorganic halide perovskites have become exceptional materials.[15] The common formula for all perovskites is ABX_3, where A represents for aliphatic or aromatic ammonium, B represents a divalent metal cation (Ni^{2+}, Cu^{2+}, Fe^{2+}, Co^{2+}, Cr^{2+}, Mn^{2+}, Cd^{2+}, Pd^{2+}, Sn^{2+}, Ge^{2+}, Eu^{2+}, Yb^{2+} or Pb^{2+}), and X is I^-, Br^- or Cl^-.[16] According to Kojima et al. (2009), halide perovskite ABX_3 (A: organic $CH_3NH_3^+$; B: Pb, and X: Br, I) has a PCE of 3.8%.[17] Subsequently, in-depth studies on materials, deposition methods, manufacturing processes, and device architecture were carried out by Yang et al. (2015) and Yin et al. (2015), improving the PCE to 20.1% experimentally and 31.4% theoretically.[18]

PSCs' instability owing to the inclusion of organic materials has been a significant concern despite their exceptional performance. Researchers have attempted to combine organic ions with other inorganic ions (e.g., Cs^+) to solve this problem. The first Cs-based perovskite, $CsSnI_3$, with Schottky solar cells, was published in 2012 with a PCE of 0.88%.[19] Since then, considerable efforts have been made to improve the performance of $CsPbI_3$-based PSC. Although $CsPbI_3$ has an efficiency of 13.21% and a suitable energy band gap of 1.73 eV,[20] it quickly deteriorates into the yellow, non-perovskite phase d-$CsPbI_3$, demonstrating poor phase stability at room temperature.[20]

Among these halide perovskites, $CsPbBr_3$ is commonly produced by reacting in the same quantities of $PbBr_2$ and CsBr using traditional wet procedures, while a few investigations have used dry approaches.[21,22] On the other hand, hybrid halide perovskites produced using solvent-free solid-state techniques exhibit considerably lower phase separation and more consistent compositions.[23] Conventional solution-based procedures have been used to successfully synthesize the novel halide compounds, β-$RbCdI_3 \cdot H_2O$, and $CsCdI_3 \cdot H_2O$.[24] The space group Pc (no. 7) is present in the monoclinic crystal structure of both substances.[24] Relatively rare, this post-perovskite structure is seen in just a few oxides, such as $MgGeO_3$,[25] $MnGeO_3$,[26] and $CaIrO_3$.[27] An example of the anti-post-perovskite structure is the Cr_3GeC compound's cubic

$Pm3m$ symmetry.[28] Specific heat measurements and differential scanning calorimetry (DSC) have corroborated the discovery of a structural phase transition at a critical temperature of 254 K.[16] Numerous studies have been conducted on the optical properties of perovskite materials[29,30] to theoretically evaluate their physical properties for various uses. Owing to their superior optoelectronic properties, such as direct band gaps, high absorption coefficients, extended carrier lifetimes, and high carrier mobilities, lead (Pb) PSCs have higher efficiencies than other PSCs.[31,32] Nonetheless, the enhanced efficiency has substantial drawbacks, including unstable device performance, lead poisoning, and shorter shelf life due to volatile organic cations and hygroscopic.[33] Finding a feasible replacement for Pb-based halide perovskites is therefore essential. Several investigations are underway to create new perovskite materials that might provide even greater or comparable high PCE. In contrast to conventional absorbers, which have less desirable or even undesirable characteristics, lead-based perovskites offer superior qualities in terms of environment, economy, and energy. The efficiency of lead-free perovskites and their potential to address the problem of Pb-based hybrid perovskites have attracted the interest of photovoltaic (PV) researchers, and $CsCdI_3$ may be a good substitute because of its favorable optoelectronic properties, high stability, and potential as an absorber layer in solar cells,[34,35] where Pb-based perovskites face both toxicity and instability issues.[36]

Numerical simulations have been employed in previous studies, and the findings were astounding. A lead-free PSC structure with a PCE of 19.03% was developed by Jabar et al.[34] With a PCE of 19.03%, the compact CdTe/$CsCdI_3$/SnO_x configuration was proposed by Jabar et al. as a new perovskite solar cell structure,[34] highlighting the necessity for more absorber tuning. Electron injection from the absorber layer is made possible by the ETL, which is also referred to as the electron collecting or extraction layer. The electrode then collects the electrons transmitted by electron-transporting materials (ETM). A composite photo-electrode can occasionally be used instead of an ETL to reduce series resistance in order to increase the efficiency of charge collection.[37] TiO_2 has been the most popular ETL in PV research because of its exceptional PV qualities.[38–41] Although there might be other options for TiO_2 as an ETL, the performance can be improved by optimizing the extraction, transformation, and load (ETL) operations. However, the HTL often aids in the extraction and transmission of holes from the absorber layer to the electrode. It also serves as an energy barrier, keeping electrons from flowing toward the anode.[42] Typically, when the band structures of heterojunction solar cells match those of the absorber layer, they operate more effectively. The excellent PV qualities and advantageous bandgap of spiro-OMeTAD make it a popular HTL.[43] Together with spiro-OMeTAD, several HTLs, such as CdTe, MoS_2, Cu_2O, CBTS, CuI, V_2O_5, PEDOT:PSS, P_3HT, and spiro-MeOTAD can be employed by aligning the band with the absorber layer under investigation.

In this study, the SCAPS-1D simulation software is used in order to optimize the optoelectronic parameters of $CsCdI_3$-

based PSCs. There are four sections of this study. Device modeling is described in Section 1. A full explanation of the simulation procedure, together with the parameters of the devices and materials utilized in the simulations, is provided in Section 2. Section 3, presents the results of adjusting the BMC of the ITO/ZnO/CsCdI$_3$/MoS$_2$/Ni solar cell structure, presents the results. Under HTL-connected conditions, we also investigated the impact of defect density and absorber layer thickness. Furthermore, we optimized the thickness of the ETL and HTL and investigated the effects of their thickness. Following optimization, the six most promising devices were explored to determine the effects of the series-shunt resistance and temperature on their performance. Finally, we explored the final optimized devices in a six-device study using Nyquist, as well as the generation recombination rate, capacitance, MS characteristics, J–V characteristics, and QE. The conclusions drawn from these observations are presented in Section 4. Our study offers a distinctive and cost-effective method for fabricating high-performance PSCs.

Finally, the findings of this study were compared and confirmed against those of earlier studies using CsCdI$_3$ absorber-based PSC devices. The manufacture and commercialization of solar cells will enter a new era with the introduction of lead-free double perovskite CsCdI$_3$.

2. Design of the proposed device

2.1. SCAPS-1D numerical simulation

We can study the principles of solar cells and identify important factors affecting their efficiency using a computational model framework. SCAPS-1D can successfully solve critical equations involving one-dimensional semiconductors using numerical techniques.[4,44] Eqn (1) illustrates how the electrostatic potential and charges are related by Poisson's equation.[45]

$$\frac{d^2}{dx^2}\psi = \frac{q}{\varepsilon_0 \varepsilon_r}\left[p(x) - n(x) + N_d - N_A + \rho_p - \rho_n\right] \quad (1)$$

In eqn (1), ψ is the electronic potential, ε_r is the relative permittivity, ε_0 for the permittivity of free space, n and p are the electron and hole densities, N_A and N_D are the densities of ionized acceptors and donors, ρ_p and ρ_n are the hole and electron distributions, and q is the electronic charge, respectively. It is recognized as the main governing equation because the continuity equation simultaneously takes into account recombination, generation, drift, and diffusion. The continuity equations illustrating variations in electron and hole concentration are shown in the eqn (2) and (3).

$$\frac{\partial n}{\partial t} = \frac{1}{q}\frac{\partial J_n}{\partial x} + (G_n - R_n) \quad (2)$$

$$\frac{\partial p}{\partial t} = \frac{1}{q}\frac{\partial J_p}{\partial x} + (G_p - R_p) \quad (3)$$

In eqn (2), and (3), the current densities of holes and electrons are indicated by J_p and J_n, respectively, whereas G_p and G_n represent the holes and electrons generation rates, and R_p and R_n represent the combination rates of holes and electrons. The

drift-diffusion equations for charge carriers are utilized to measure the hole and electron current densities in the SCs, as shown in eqn (4) and (5), respectively:

$$J_n = q\mu_n n\varepsilon + qD_n\partial n \quad (4)$$

$$J_P = q\mu_P p\varepsilon + qD_P\partial p \quad (5)$$

The carrier mobility is represented by μ_n and μ_p in eqn (4) and (5), while D_n and D_p represent the diffusion coefficients of electrons and holes, respectively. The diffusion coefficient depends on the mobility and lifespan of the carrier, as explained by Einstein's relationship.[46] Additionally, the updated $E_{g\text{-sqrt}}$ model, a modified version of the traditional sqrt($hv - E_g$) model, was used to compute the absorption constant for the films. As seen below, eqn (6) illustrates how the "Tauc laws" represent this relationship.

$$\alpha(hv) = \left(\alpha_0 + \beta_0\frac{E_g}{hv}\right)\sqrt{\frac{hv}{E_g} - 1} \quad (6)$$

Here in eqn (6), the photon energy is represented by hv, the bandgap is denoted by E_g, and α stands for the absorption coefficient. The eqn (7) and (8) connect the relationship between the model constants α_0 and β_0 to the conventional model constants A and B, as shown below, respectively:

$$\alpha_0 = A\sqrt{E_g} \quad (7)$$

$$\beta_0 = \frac{B}{\sqrt{E_g}} \quad (8)$$

Under steady-state circumstances, SCAPS-1D evaluates the basic semiconductor equations. Fig. 1 shows the SCAPS-1D simulation procedure. CsCdI$_3$ as the perovskite absorber, PCBM, LBSO, SnS$_2$, IGZO, WS$_2$, and ZnO as ETLs, MoS$_2$ as the HTL, and Ni as the BMC were among the layers used to define the solar cell structure once the SCAPS-1D simulation was started. Material parameters (bandgap, electron affinity, dielectric permittivity, effective density of states, thermal velocity, carrier mobilities, defect density, *etc.*) and operating
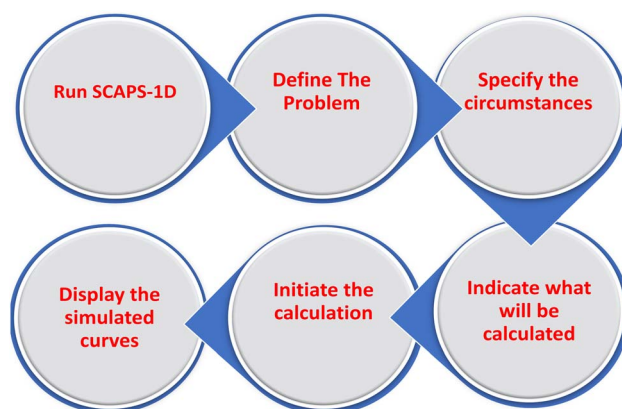

Fig. 1 Running procedure SCAPS-1D.

conditions (temperature, bias voltage range for $J–V$ characteristics, and illumination intensity AM1.5G) were provided as inputs. Several measures were taken into consideration, such as Mott–Schottky characteristics, capacitance, QE, and $J–V$ characteristics. Subsequently, the simulation was started, containing solutions to the drift-diffusion equations, continuity equations, and Poisson's equation. The performance of the solar cell was assessed using graphical tools such as Origin.

2.2. CsCdI₃-based PSC structure

A schematic device architecture of the CsCdI₃-based PSC structure and crystal structure are illustrated in Fig. 2(a) and (c), respectively. ETLs, HTL, BMC, and CsCdI₃ absorber layers were integrated to construct a CsCdI₃-based PSC. The CsCdI₃ absorber's solar cell structure results in an n–i–p structure. The depletion zone of the n–i–p structure extends throughout the intrinsic region, significantly outperforming conventional p–n junctions for long-wavelength response applications. This architectural design enables deeper photon penetration into the semiconductor material, whereas traditional configurations restrict current generation to electron–hole pairs formed primarily at the immediate junction interface. The substantially expanded junction region dramatically enhances the cell's QE
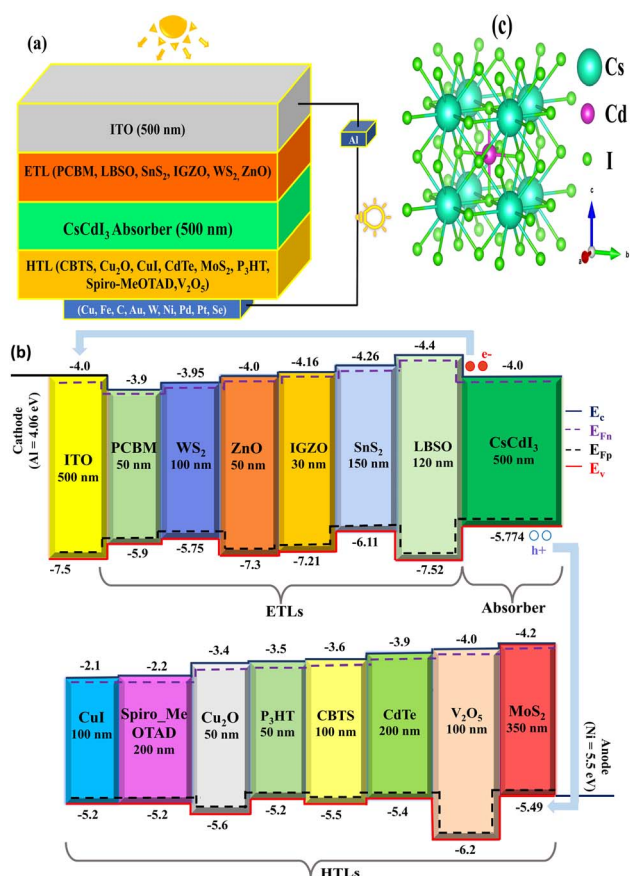

Fig. 2 (a) Schematic device structure, (b) energy band level alignment of the related (a) ITO, ETLs, and absorber CsCdI₃, and (b) HTLs, and (c) crystal structure.

Table 1 Data table of input parameters used for TCO, ETLs, and CsCdI₃ (absorber layer)

Parameter (unit)	ETL							Absorber
	ITO[14]	LBSO[47]	SnS₂ (ref. 47)	PCBM[14]	IGZO[14]	WS₂ (ref. 14)	ZnO[14]	CsCdI₃ (ref. 34)
Thickness (nm)	500	120	150 (ref. 48 and 49)	50	30	100	50	500
Bandgap, E_g (eV)	3.5	3.12	1.85	2	3.05	1.8	3.3	1.774
Electron affinity, X (eV)	4	4.4	4.26	3.9	4.16	3.95	4	4
Relative dielectric permittivity, ε_r	9	22	17.7	3.9	10	13.6	9	10.00
CB effective density of states, N_C (cm^{-3})	2.2×10^{18}	1.8×10^{20}	7.32×10^{18}	2.5×10^{21}	5×10^{18}	10^{18}	3.7×10^{18}	2.2×10^{18}
VB effective density of states, N_V (cm^{-3})	1.8×10^{19}	1.8×10^{20}	10^{19}	2.5×10^{21}	5×10^{18}	2.4×10^{19}	1.8×10^{19}	1.8×10^{19}
Electron thermal velocity (cm s^{-1})	10^7	10^7	10^7	10^7	10^7	10^7	10^7	10^7
Hole thermal velocity (cm s^{-1})	10^7	10^7	10^7	10^7	10^7	10^7	10^7	10^7
Electron mobility, μ_n (cm^2 V^{-1} s^{-1})	20	0.69	50	0.2	15	100	100	10^2
Hole mobility, μ_h (cm^2 V^{-1} s^{-1})	10	0.69	25	0.2	0.1	100	25	2.5×10^1
Shallow uniform donor density, N_D (cm^{-3})	10^{21}	2×10^{21}	9.85×10^{19}	2.93×10^{17}	10^{17}	10^{18}	10^{18}	1.1×10^{18}
Shallow uniform acceptor density, N_A (cm^{-3})	0	0	0	0	0	0	0	0
Defect density, N_t (cm^{-3})	10^{15}	10^{14}	10^{14}	10^{15}	10^{15}	10^{15}	10^{15}	10^{15}

Table 2 Data table of input parameters for HTLs

Parameter (unit)	CBTS[32]	Cu$_2$O[32]	CuI[32]	CdTe[47]	MoS$_2$ (ref. 50)	P$_3$HT[32]	Spiro_MeOTAD[32]	V$_2$O$_5$ (ref. 32)
Thickness (nm)	100	50	100	200	350 (ref. 51)	50	200	100 (ref. 14 and 52)
Bandgap (eV)	1.9	2.2	3.1	1.5	1.29	1.7	3	2.20
Electron affinity (eV)	3.6	3.4	2.1	3.9	4.2	3.5	2.2	4.00
Dielectric permittivity (relative)	5.4	7.5	6.5	9.4	3	3	3	10.00
CB effective density of states (cm^{-3})	2.2×10^{18}	2×10^{19}	2.8×10^{19}	8×10^{17}	2.2×10^{18}	2×10^{21}	2.2×10^{18}	9.2×10^{17}
VB effective density of states (cm^{-3})	1.8×10^{19}	10^{19}	10^{19}	1.8×10^{19}	1.8×10^{19}	2×10^{21}	1.8×10^{19}	5.0×10^{18}
Electron thermal velocity (cm s^{-1})	10^7	10^7	10^7	10^7	10^7	10^7	10^7	10^7
Hole thermal velocity (cm s^{-1})	10^7	10^7	10^7	10^7	10^7	10^7	10^7	10^7
Electron mobility, μ_n (cm^2 V^{-1} s^{-1})	30	200	100	3.2×10^2	100	1.8×10^{-3}	2.1×10^{-3}	3.2×10^2
Hole mobility, μ_h (cm^2 V^{-1} s^{-1})	10	8600	43.9	4×10^1	150	1.86×10^{-2}	2.16×10^{-3}	4×10^1
Shallow uniform donor density, N_D (cm^{-3})	0	0	0	0	0	0	0	0
Shallow uniform acceptor density, N_A (cm^{-3})	10^{18}	10^{18}	10^{18}	2.0×10^{14}	10^{18}	10^{18}	10^{18}	10^{18}
Defect density, N_t (cm^{-3})	10^{15}	10^{15}	10^{15}	10^{15}	10^{15}	10^{15}	10^{15}	10^{15}

by facilitating more effective mechanisms for both generating and separating electron–hole pairs.[14] The sophisticated CsCdI$_3$ absorber heterostructure demonstrated exceptional light-harvesting capabilities while ensuring that the heavily doped HTL and ETL functioned optimally as ohmic contacts. This arrangement simultaneously accomplishes two critical functions: efficient charge carrier management and effective photon retention within the active region, resulting in superior photo-electric conversion performance across the targeted wavelength spectrum. The software helped us analyze the performance of various single PSC structures throughout the SCAPS-1D inquiry.

These perovskite structures were formed by setting the frequency at 1 MHz, the ambient temperature at 300 K, and using the AM1.5G sunlight spectrum. Furthermore, six ETLs (PCBM, LBSO, SnS$_2$, IGZO, WS$_2$, and ZnO), ten as HTLs (MoS$_2$, Cu$_2$O, CBTS, CdTe, V$_2$O$_5$, spiro-MeOTAD, CuI, and P$_3$HT), and ten as BMCs (Cu, Fe, C, Au, W, Ni, Pd, Pt, and Se) were initially established through a variety of studies to investigate the differences in their architectures and optoelectronic characteristics, which are presented in Tables 1–3.

2.3. Band alignment of CsCdI$_3$-based absorber with different ETLs

Fig. 2b depicts the band alignment of several heterostructures utilizing the CsCdI$_3$ absorber. The quasi-Fermi levels of electrons (F_n) and holes (F_p) are shown, together with the conduction valence band maxima (E_V) and band minima (E_C). While F_n and E_C have a harmonic relationship, F_p aligns with E_V in each type of ETL. Additionally, F_n intersects E_C and stops the flow of electrons from the HTL and holes from the ETLs because MoS$_2$ as the HTL, E_V, and F_p stay at the same level. To get around this, electrons are effectively collected using an ITO front contact with a work function (WF) of 3.5 eV, while a nickel (Ni) back contact is much less expensive than other valuable contacts (Ag, Au, Pt, Pd, and Se) that have stability, enhanced photostability, and high efficiency.

3. Results and discussion

3.1. Optimization of CsCdI$_3$-based solar cell

3.1.1. Structural stability of CsCdI$_3$-based solar. The geometric and structural stability of the single halide perovskite CsCdI$_3$ was assessed using three widely recognized descriptors: the tolerance factor (t), the octahedral factor (μ), and the revised tolerance factor (τ). These stability indices provide essential guidelines for predicting whether the material can adopt a cubic perovskite framework suitable for photovoltaic applications. The goldschmidt tolerance factor (t) evaluates how well the ionic sizes of the A-site cation, the B-site cation, and the halide anion fit into the perovskite lattice, thereby indicating the feasibility of forming a symmetric cubic structure. The octahedral factor (μ) relates to the geometric stability of the octahedra, highlighting the degree of distortion within the crystal lattice. Meanwhile, the newer tolerance factor (τ) provides an advanced measure that accounts for oxidation states and radius ratios,

Table 3 Data table of interfacial properties employed in this CsCdI$_3$-based PSC[53]

Interface	Type of defect	Capture cross section: electrons/holes (cm^2)	Energetic distribution	Reference for defect energy levels, E_t	Total density (cm^{-2})
ETL/CsCdI$_3$	Neutral	10^{-17} 10^{-18}	Single	Above the VB maximum	10^{10}
CsCdI$_3$/HTL	Neutral	10^{-18} 10^{-19}	Single	Above the VB maximum	10^{10}

offering improved predictive accuracy under different structural conditions.

The stability factors are calculated using the following relations: eqn (9)–(11)[54–56]

$$\tau = \frac{R_X}{R_B} - n_A\left(n_A - \frac{R_A}{R_B}\right) \quad (9)$$

$$t = \frac{R_A + R_X}{\sqrt{2}(R_A + R_X)} \quad (10)$$

$$\mu = \frac{R_B}{R_X} \quad (11)$$

where R_A and R_B correspond to the effective ionic radii of the A-site and B-site cations, R_X is the halide anion radius, and n_A is the oxidation state of the A-site cation. For double perovskites (A$_2$B′B″X$_6$), the effective B-site radius is calculated as an average, but in single perovskites such as CsCdI$_3$, R_B directly corresponds to Cd^{2+}.

A perovskite is generally considered cubic if t falls within 0.813–1.107 (ref. 55) and μ lies between 0.41–0.89.[56] Furthermore, a τ value below 4.18 also signifies stable cubic formation.[54] Using Shannon's ionic radii, Cs$^+$ (CN = 12, 1.88 Å), Cd^{2+} (CN = 6, 0.95 Å), and I$^-$ (CN = 6, 2.20 Å), the calculated values for CsCdI$_3$ are: $t = 0.916$, $\mu = 0.432$, and $\tau = 4.215$, illustrated in Table 4.

All three parameters reside within the accepted stability ranges, confirming that CsCdI$_3$ is structurally favorable for the cubic perovskite phase. Shannon's standard radii database is used for the ionic radii required for these calculations.[57]

3.1.2. BMC optimization. In this section, we focus on optimizing the BMC of the ITO/ETL/CsCdI$_3$/MoS$_2$/BMCs solar cell structure, which is illustrated in Fig. 3. Nine BMC work function modifications were made to enhance the output parameters of the PSC. Work function ratings were used to classify metals. The shunt resistance and performance of a device are known to decrease with the work function of the contact metal. The performance was particularly lower than that of the other BMCs when Cu was utilized as the BMC. Cu has

serious stability issues in addition to its low work function. When Cu and Fe are used as BMCs with high work functions, the perovskite-HTM-BMC interfaces experience advantageous band bending. This provides an effective barrier to electron transfer from perovskite to metal, and the high R_{sh} value reduces the alternative current path previously created by the low R_{sh} value. Furthermore, these metals exhibit minimal interfacial resistance to HTM. Nevertheless, the back contact work function is larger than that of the previously stated BMCs, and the solar cell performance remains almost constant. This is because increasing the work function ratings enhances R_{sh} and removes the alternating current channel for the current generated by light. A lower work function results in a higher FF value owing to a decrease in the reverse saturation current. For example, in Fig. 3(f), utilizing ZnO-ETL, BMC using Se, Pt, and Pd shows a PCE of 26.736%, 26.73% and 26.62%, whereas Ni showed a PCE of 25.06% and an FF of 87.137%. However, because Ni is more affordable than Se, Pt, and Pd, it appears to be a more effective BMC material. Therefore, the solar cell arrangement using Ni as a BMC appears to be more efficient than that using the other BMCs. Finally, the best-performing device configuration was ITO/ZnO/CsCdI$_3$/MoS$_2$/Ni, which exhibited the highest performance, with a PCE of 25.05032%, V_{OC} of 0.93616 V, J_{SC} of 30.7086 mA cm^{-2}, and FF of 87.13735% as shown in Fig. 3(f). To effectively capture holes *via* the BMC, it is necessary to build an ohmic contact.[58] Here, Al is used as the right contact with a work function value of 4.06 eV.[59] Furthermore, the work function of the BMCs (Cu, Fe, C, Au, W, Ni, Pd, Pt, and Se) used in this study were 4.65, 4.81, 5, 5.1, 5.22, 5.5, 5.6, 5.7, and 5.9, respectively.[59,60] The simulation began with Au as the BMC. However, when the BMC was adjusted, substantial changes in the performance characteristics were evident in the energy band diagram owing to the presence of a Schottky barrier.

3.1.3. HTL and ETL optimization. To identify which HTL and ETL were best for the optimizations, eight HTLs and six ETLs were merged with the absorber layer, and Ni BMC was used as a reference to create 48 distinct structures ITO/ETLs/CsCdI$_3$/

Table 4 Shannon's ionic radii (r), goldschmidt tolerance factor (t), octahedral factor (μ), and new tolerance factor (τ) for CsCdI$_3$

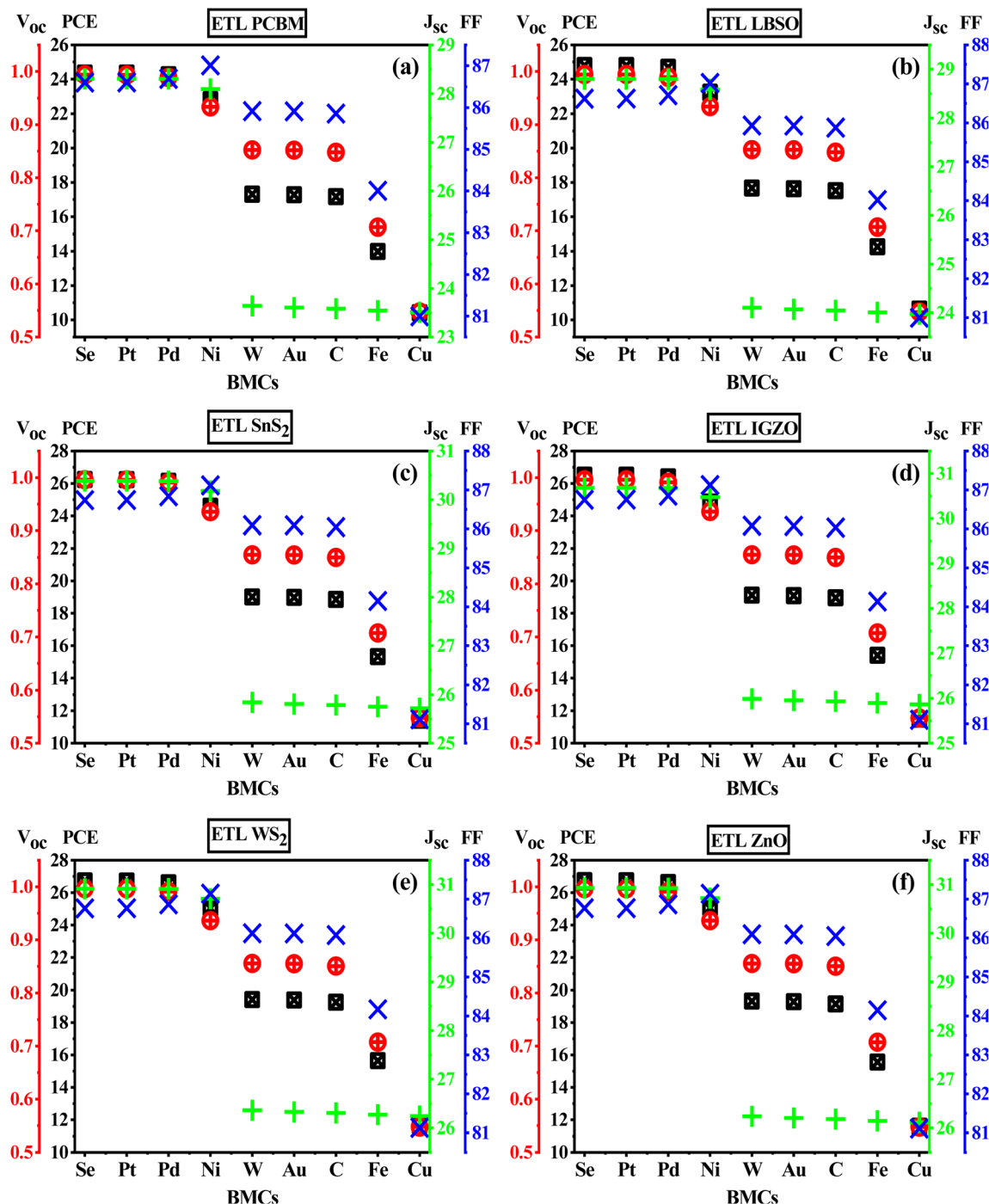| DP	The ionic radius of cations (Å)		The ionic radius of the anion (Å)	Goldschmidt tolerance factor (t)	Octahedral factor (μ)	New tolerance factor (τ)
	R_A	R_B	R_X			
CsCdI$_3$	1.88	0.95	2.20	0.916	0.432	4.215

Fig. 3 Influence of various BMCs in the structure of ITO/ETL/$CsCdI_3$/MoS_2/BMCs, where (a) PCBM, (b) LBSO, (c) SnS_2, (d) IGZO, (e) WS_2, and (f) ZnO are used as ETL.

HTLs/Ni. The change in PV attributes such as V_{OC}, J_{SC}, FF, and PCE for distinct HTLs and ETLs are depicted in Fig. 4(a–d). In Fig. 4a, Cu_2O HTL, as well as WS_2 and ZnO ETLs, showed the highest V_{OC} of 1.46 V. Fig. 4b illustrates that MoS_2 HTL, as well as WS_2 and ZnO ETLs, showed the highest J_{SC} of 30.7 mA.cm^{-2}. Fig. 4c shows that the Cu_2O HTL and WS_2 ETL exhibit the highest FF of 89.58%. Furthermore, Fig. 4d shows that the MoS_2 HTL and ZnO ETL exhibited the highest PCE of 25.06%.

In conclusion, MoS_2 shows the best performance as an HTL compared to the other HTLs in most cases with different ETLs. This can be attributed to its exceptional characteristics, including excellent conductivity, which improves the collection mechanism and appropriate band alignment, which protects the device performance from the interfacial trap effect. According to analysis, MoS_2 is chosen as HTL as well as ZnO is chosen as ETL, and the structure ITO/ZnO/$CsCdI_3$/MoS_2/Ni

Fig. 4 Impact of various HTL and ETL in PSC while Ni is used as BMC in the structure of ITO/ETLs/CsCdI$_3$/HTLs/Ni. (a) V_{OC}, (b) J_{SC}, (c) FF, and (d) PCE.

provides the best PCE among other configurations with other HTLs, and ETLs of around 25.06%, and it also displays the best J_{SC} of around 30.7 mA cm^{-2} compared to other HTLs, and ETLs. Concerning the device's efficiency and other PSC parameters, MoS$_2$ and ZnO were utilized as the ideal HTL and ETL, respectively, for the enhancement of the absorber.

3.1.4. Band structure of CsCdI$_3$ configurations with different ETLs. Fig. 5(a–f) illustrates the band alignment of the PSC structure ITO/ETL/CsCdI$_3$/MoS$_2$/Ni for six distinct ETLs. Each ETL with a CsCdI$_3$ absorbing layer and MoS$_2$ as the HTL affects the valence/conduction band offset, or the difference in the valence band between the absorber layer and HTL in the energy band diagram. The performance and efficiency of PSCs are significantly affected by the alignment of the energy levels. The photogenerated holes and electrons were injected into the ETL conduction band and moved to the HTL in the PSCs. Following photoelectric conversion, the generated charge carriers—electrons and holes accumulate in the BMC and ITO layers. The energy band alignment disparities at the CsCdI$_3$/HTL and ETL/CsCdI$_3$ interfaces significantly influence the overall device performance. The interface parameters directly determine the extent of recombination effects at these critical boundaries, highlighting the necessity for precise optimization of the electrical properties of the HTL and ETL. The device architecture shown in Fig. 5(e and f), uses MoS$_2$ as the HTL and WS$_2$ and ZnO as the ETL, revealing a distinctive conduction band (E_c) behavior relative to the Fermi level (F_n). Initially, E_c positions above F_n, then converges with F_n at approximately 0.3 μm depth, before transitioning below F_n by the remaining 0.5 μm region. Similar E_c behavior patterns emerge across the alternative CsCdI$_3$-based configurations depicted in Fig. 5(a–d), which implement PCBM, LBSO, SnS$_2$, and IGZO as ETL materials while maintaining MoS$_2$ as the HTL. These configurations were consistently demonstrating the characteristic progression where E_c begins above F_n, remains marginally higher than F_n beyond 0.2 μm thickness, and subsequently positions below F_n

through the final 0.5 μm section. The band gaps of the PCBM, LBSO, SnS$_2$, IGZO, WS$_2$, and ZnO ETLs were 2, 3.12, 1.85, 3.05, 1.8, and 3.3 eV, respectively. In Fig. 5(a–f), F_p is constantly located above the E_V for all the ETL.

For efficient electron extraction at the ETL/CsCdI$_3$ junction, the ETL must possess a higher electron affinity than CsCdI$_3$. Conversely, effective hole collection at the CsCdI$_3$/HTL interface requires the MoS$_2$ HTL to maintain a lower electron affinity than that of CsCdI$_3$. The device performance metrics are critically influenced by the energy-band discontinuities occurring at both interfaces. Under thermal equilibrium conditions, F_n was uniform throughout the entire structure. This equilibrium is disrupted when photons interact with the PSC architecture, thereby generating distinct quasi-Fermi energy levels.

The MoS$_2$ layer's higher electron affinity relative to that of the CsCdI$_3$ absorber facilitates efficient hole collection at the CsCdI$_3$/MoS$_2$ boundary. This advantageous extraction mechanism operates at the interfaces between CsCdI$_3$ and various ETMs, including PCBM, LBSO, SnS$_2$, IGZO, WS$_2$, and ZnO, enabling effective charge carrier separation and transport throughout the device structure. Owing to the well-aligned and nearly similar alignment of the energy band, the devices may offer a good efficiency of around 25%. In line with previous studies on CsCdI$_3$ perovskites, the study found that increasing the thickness of the absorber layer decreases the efficiency of the device structures.[34]

3.1.5. Effects of VBO and CBO. In perovskite solar cells (PSCs), the ETL and HTL are essential for efficiently directing photo-generated charge carriers from the perovskite absorber to their respective electrodes. Beyond simply guiding charges, these transport layers act as selective barriers, preventing unwanted electrons and holes from migrating to incorrect regions at the ETL/absorber and HTL/absorber interfaces, thereby minimizing interfacial recombination losses.[61] Upon illumination, the perovskite layer generates electron–hole pairs, which are then separated and directed toward the appropriate contacts. The effectiveness of this process is largely determined by the energy band alignment at these interfaces, specifically the conduction band offset (CBO) and valence band offset (VBO), which directly influence carrier extraction efficiency and the overall power conversion performance of the device.

The CBO at the ETL/absorber interface is calculated as:

$$\text{CBO} = \chi_{\text{absorber}} - \chi_{\text{ETL}} \tag{12}$$

where χ_{absorber} and χ_{ETL} are the electron affinities of the absorber and ETL, respectively. Depending on the relative positions of the conduction band minima (CBM), three types of alignments can occur: (1) cliff-like (negative CBO): arises when ($\chi_{\text{ETL}} > \chi_{\text{absorber}}$), forming a downward energy step that can promote electron recombination. (2) Flat-band (CBO = 0): ideal alignment with no energy barrier, allowing smooth electron transfer, and (3) spike-like (positive CBO): occurs when ($\chi_{\text{ETL}} < \chi_{\text{absorber}}$), creating an upward barrier that may partially hinder electron transport.

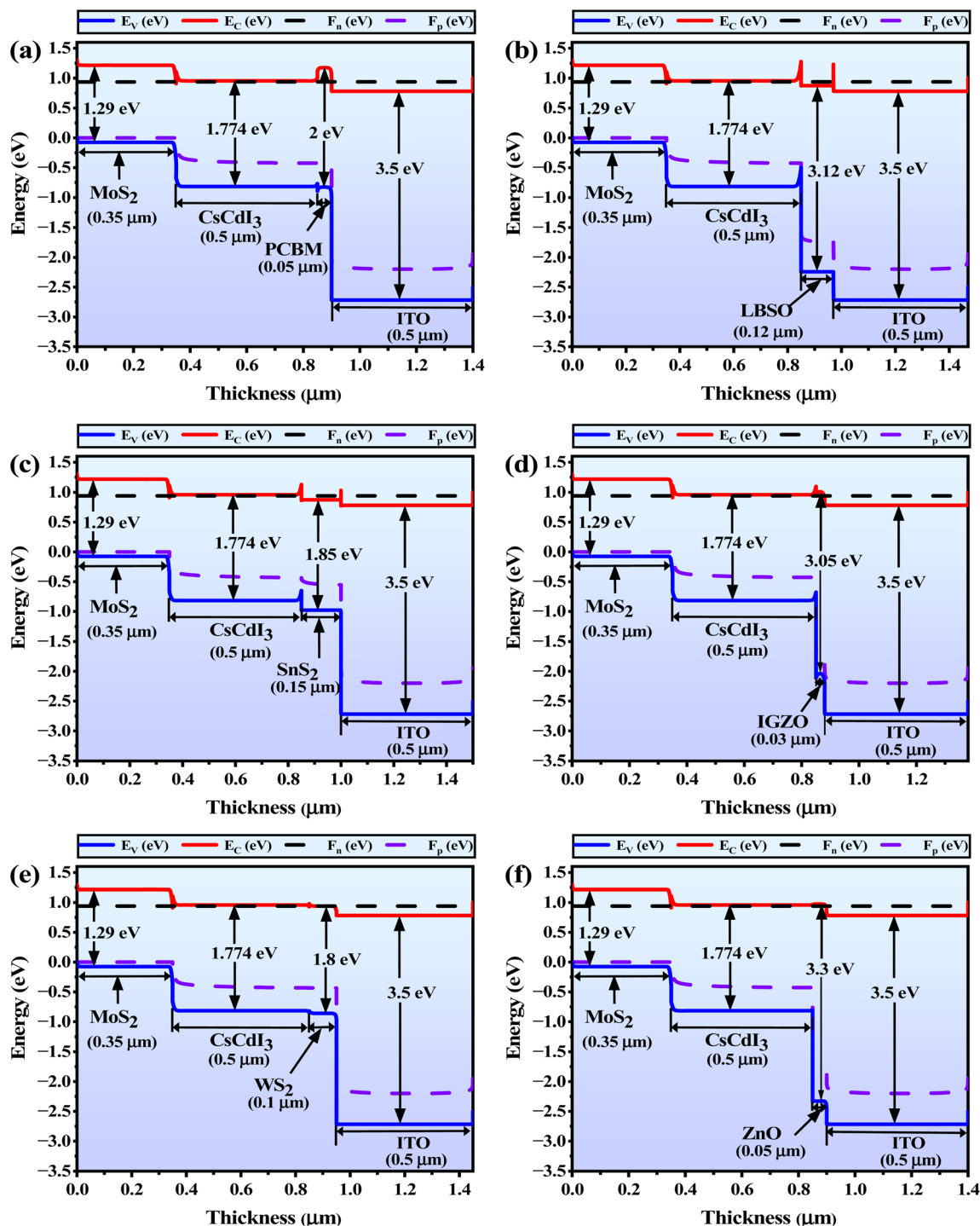Similarly, the VBO at the absorber/HTL interface can be expressed as:

Fig. 5 Band diagrams of the various ETL materials based on the structure of ITO/ETL/CsCdI$_3$/MoS$_2$/Ni, where (a) PCBM, (b) LBSO, (c) SnS$_2$, (d) IGZO, (e) WS$_2$, and (f) ZnO are used as ETL.

$$VBO = \chi_{HTL} - \chi_{absorber} + E_{g.HTL} - E_{g.absorber} \quad (13)$$

Here, $E_{g.HTL}$ and $E_{g.absorber}$ denote the band gaps of the HTL and absorber, respectively. The VBO determines the efficiency of hole transport: negative VBO (cliff-like): occurs when the HTL's valence band maximum (VBM) is higher than the absorber's, potentially affecting hole collection, zero VBO (flat-band):

perfect alignment that facilitates efficient hole transfer and positive VBO (spike-like): arises when the absorber's VBM is higher than the HTL's, creating a barrier that can impede holes. We calculated the VBO and CBO through the eqn (12) and (13).[61] For example, in a CsCdI$_3$-based PSC with ZnO as the ETL, the CBO is calculated as: CBO = 4.146–3.95 = 0.196 eV, indicating a spike-like barrier. At the HTL interface, the VBO is: VBO =

Table 5 Calculated VBO and CBO values for six distinct ETL with absorber CsCdI₃

Absorber	ETLs Six ETLs	CBO Values	Comment (barrier)	VBO Values	Comment (barrier)
CsCdI₃	ZnO	0	Flat-band	−0.284	Cliff-like
	WS₂	0.05	Spike-like		
	PCBM	0.1			
	SnS₂	−0.26	Cliff-like		
	IGZO	−0.16			
	LBSO	−0.4			

4.2 eV − 4 eV + 1.29 eV − 1.774 eV = −0.284 eV, which corresponds to a cliff-like barrier. Table 5 summarizes the estimated CBO and VBO values for various ETLs, illustrating the impact of interface energetics on charge transport and device efficiency.

3.2. Optimization of absorber and ETL thickness

3D plot mapping techniques were employed to investigate how the thicknesses of both the absorber and various ETLs influence the performance parameters across six different single-halide perovskite solar cell configurations. Selection of the appropriate absorber and ETL material are essential to creating high-performance solar cells. Light capture and effective hole collection from the absorber layer are demonstrated by a layer of appropriate thickness. Using 3D plot mapping to analyze the impact of the absorber and ETL layer thickness on the performance of various solar cell designs enables the assessment of the key parameters needed for the best potential solar cell performance.

Fig. 6 3D colormap of V_{OC} when ETL is (a) PCBM, (b) LBSO, (c) SnS₂, (d) IGZO, (e) WS₂, and (f) ZnO.

Fig. 6 illustrates how variations in both absorber and ETL thicknesses affect the V_{OC} parameter across the six different solar cell configurations. As shown in Fig. 6(a), the PCBM-based device configuration was explored using ETL thicknesses ranging from 50 to 250 nm, while the absorber thicknesses varied between 400 and 1200 nm. According to research, a decrease in V_{OC} is often the result of the thickening of the absorber. However, as shown in Fig. 6(a), increases in the ETL layer thickness do not affect on V_{OC} when the absorber thickness is constant. Comparable response patterns were exhibited by the other ETL-based configurations. Fig. 6(a–f) illustrates, optimal V_{OC} values for all six ETL-based configurations were observed when the thickness of the absorber layer was between approximately 400 nm and 500 nm. For the WS$_2$ and ZnO-based structure, the highest V_{OC} was observed when the absorber thickness was around 500 nm and the ETL thickness was approximately 50 nm, as illustrated in Fig. 6(e and f). Fig. 6 demonstrates that an increased absorber layer thickness generally results in a reduced V_{OC} across most of the evaluated devices. This inverse relationship can be attributed to the enhanced carrier recombination processes occurring within

thicker absorber layers, which consequently elevate the saturation current beyond the photocurrent level.[13]

Fig. 7 depicts the effect of variations in the ETL and absorber layer thickness on the J_{SC} of six specific PSCs. Higher J_{SC} values resulted from increasing the absorber thickness while maintaining the ETL thickness constant. Increased generation rate and J_{SC} values result from improved light absorption made possible by a larger absorber layer. The effect of the series resistance can be mitigated by a thinner ETL layers, which increases the current by reducing electron–hole pair recombination. Furthermore, decreasing the ETL thickness contributes to the creation of rough surfaces and large pinholes, which can severely affect V_{OC}, J_{SC}, and overall PCE. The maximum J_{SC} performance for all configurations and ETL-based structures was consistently achieved with an absorber layer thickness of approximately 400 nm, as demonstrated in Fig. 7(a–f). Among these devices, the ZnO-based structure exhibited the highest J_{SC} values when the absorber thickness ranged from 400 to 500 nm, combined with an ETL thickness of approximately 170 nm, as shown in Fig. 7(f). A higher J_{SC} is the result of improved light absorption by the higher absorber layer, which also raises the
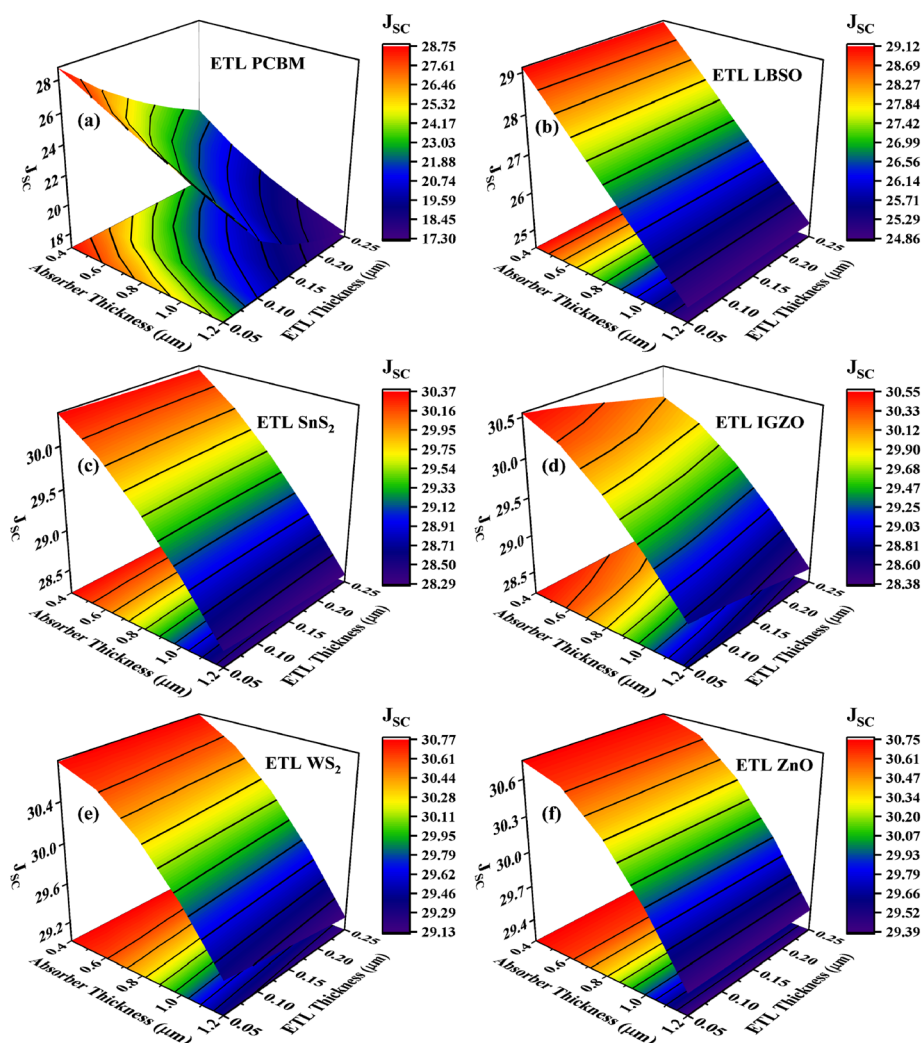

Fig. 7 3D colormap of J_{SC} when ETL is (a) PCBM, (b) LBSO, (c) SnS$_2$, (d) IGZO, (e) WS$_2$, and (f) ZnO.

generation rate.[13] By decreasing the electron–hole pair recombination, a thin ETL lowers series resistance and increases the current. Furthermore, J_{SC} can be severely hampered by the development of rough surfaces and larger pinholes, which can be avoided by decreasing the ETL thickness.[13] Fig. 8 illustrates the influence of changes in the thickness of the absorber and ETL layers on the FF values. In Fig. 8(a–c), for each of the six ETL-based solar cell designs, it is evident that the FF values decrease as the absorber layer thickness increases, while changes in the ETL layer thickness do not affect the FF values. The decrease in FF may be related to the increase in series resistance as the absorber thickness increases.[62]

For the WS$_2$, and ZnO-based devices, the highest FF was identified, when the thickness of the absorber was around 400 to 500 nm, and the thickness of the ETL was around 130 to 225 nm as shown in Fig. 8(e and f), and the value was 87.14%. Moreover, the lowest FF value was around 86.76%, as shown in Fig. 8(a). In contrast, every ETL except PCBM (Fig. 8(a)) demonstrates that the FF values decrease as the absorber and ETL thickness increase.

Thicker ETL layers lower the parasitic absorption and series resistance, improving the charge extraction and maintaining a higher FF. Furthermore, a thinner perovskite layer minimizes recombination losses by striking a balance between effective charge extraction and adequate light absorption.[53] Together, all of these factors result in increased efficiency at reduced absorber thicknesses and ETL. Fig. 9(b–f) depicts a similar pattern of declining PCE with increasing absorber layer thickness in LBSO, SnS$_2$, IGZO, WS$_2$, and ZnO ETLs-based solar cells. All ETL-based structures, with the exception of PCBM ETL Fig. 9(b–f), show the highest PCE values at absorber layer thicknesses of about 500 nm. As seen in Fig. 9(e and f), the maximum PCE is achieved in the case of the WS$_2$ and ZnO-based structure when the absorber and ETL thicknesses are around 400–500 nm and 60–220 nm, respectively. Efficiency is shown to decline with absorber thickness inclination for all device configurations for all device architectures, which is consistent with an earlier study.[63] The primary layer that collects and converts photon energy into electrical energy is the absorber layer. Fig. 6–9 shows how the absorber layer thickness
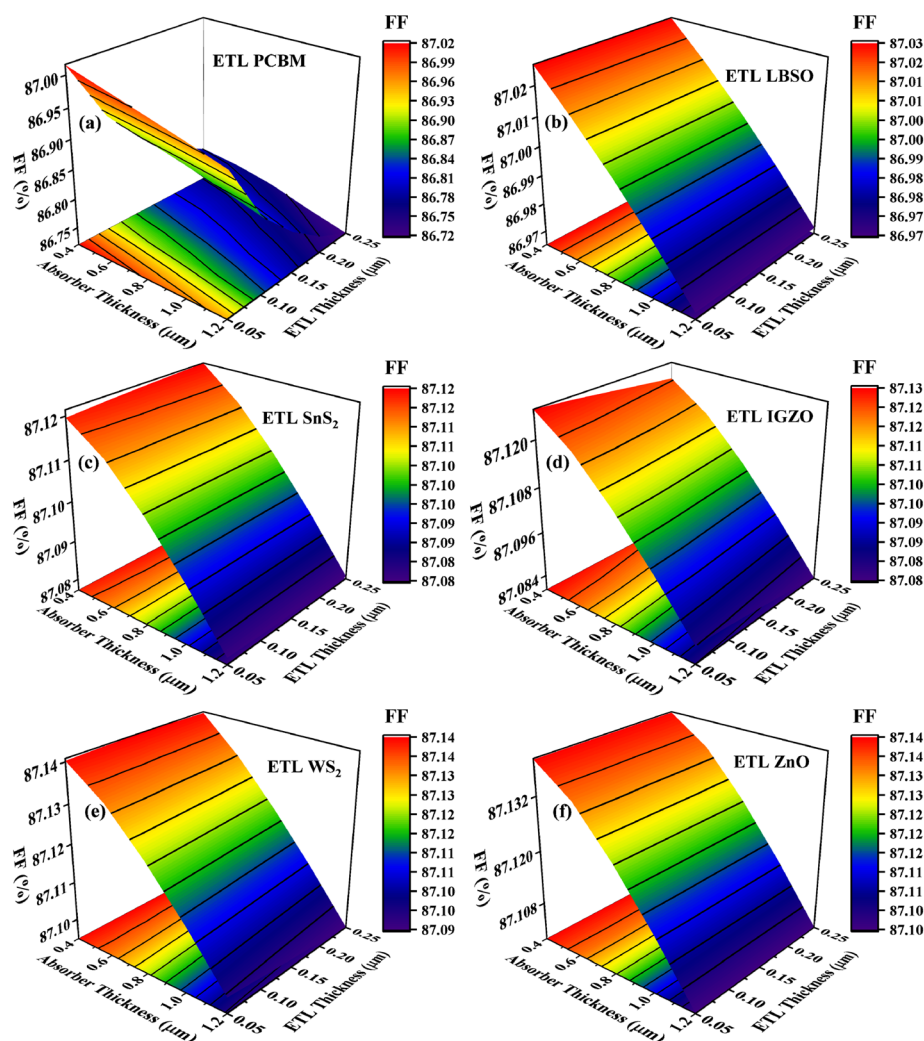

Fig. 8 3D colormap of FF when ETL is (a) PCBM, (b) LBSO, (c) SnS$_2$, (d) IGZO, (e) WS$_2$, and (f) ZnO.

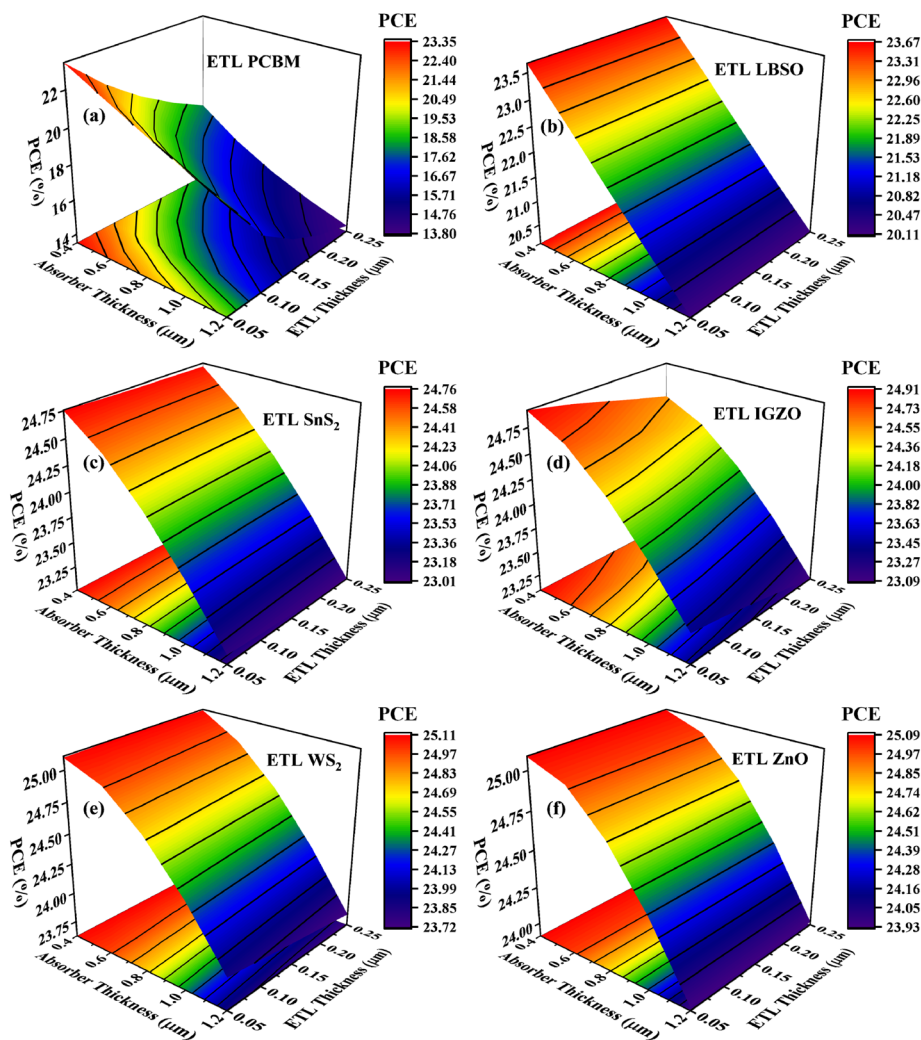© 2025 The Author(s). Published by the Royal Society of Chemistry

Fig. 9 3D colormap of PCE when ETL is (a) PCBM, (b) LBSO, (c) SnS$_2$, (d) IGZO, (e) WS$_2$, and (f) ZnO.

affects the device's performance parameters. To study the impact on V_{OC}, J_{SC}, FF, and PCE, the thickness was varied from 400 nm to 1200 nm. As the thickness of the absorber layer increases, all four characteristics begin to decline. A low thickness results in less photon absorption. However, the active layer thickened considerably. In this scenario, PCE and J_{SC} drop because there is a greater possibility that photo-excited carriers may recombine before they reach the ETL and HTL interfaces. A similar tendency was observed in a previous study.[64] Accordingly, the device PCE indicated that the absorber layer should have a thickness of 500 nm. Fig. 6–9 illustrates how varying the ETL thickness affects the key solar cell parameters: V_{OC}, J_{SC}, FF, and PCE. To achieve optimal photon transmission and device performance, ETLs are typically designed to be thinner than HTLs. This thinness requirement stems from the need to minimize light scattering, as excessive ETL thickness can impede photon penetration into the active layer, given that light encounters the ETL first in the device architecture.[64] The ETL thickness was varied between 50 and 250 nm while maintaining a constant 500 nm absorber layer to evaluate the performance parameters. The analysis revealed that most device

configurations maintained relatively stable performance parameters despite ETL thickness variations, with PCBM and LBSO being the notable exceptions. The ITO/ZnO/CsCdI$_3$/MoS$_2$/Ni structure uniquely demonstrated a slight performance enhancement with increasing ETL thickness. The ideal SnS$_2$ and LBSO thickness, taking into account manufacturing challenges and efficiency, is 150 nm and 120 nm, whereas the values for the other four ETLs are set at 50 nm, which is consistent with the previous study.[47,49]

3.2.1. Combined influence of thickness and defect density of absorber on PV performance. Photovoltaic (PV) performance is significantly affected by the absorber layer thickness, which also directly affects the solar cell (SC) performance through the absorber thickness and absorber defect density (N_t).[13] Photoelectrons are produced when light interacts with an absorber layer. Nevertheless, the ETL may not be sufficiently protected owing to the perovskite layer's poor shape.

Low-quality films increases the defect density, which leads to increased recombination.[65] Elevated N_t levels promote recombination inside the absorber layer, reducing the stability of PSCs and PCE, while also boosting pinhole development and film
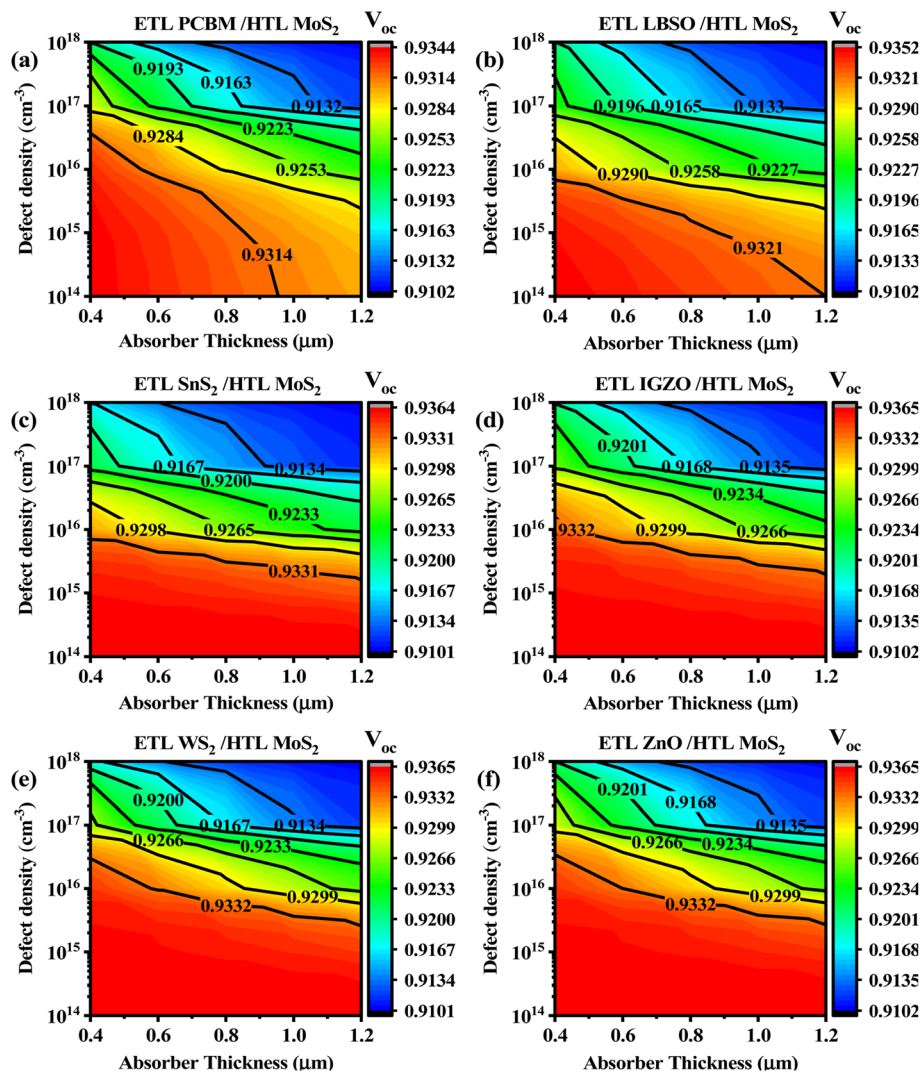
Fig. 10 Contour map of V_{OC} dependency on absorber defect density and thickness when ETL is (a) PCBM, (b) LBSO, (c) SnS$_2$, (d) IGZO, (e) WS$_2$, and (f) ZnO.

degradation.[66] Fig. 10–13 shows changes in the absorber thickness from 400 to 1200 nm and N_t from 10^{14} to 10^{18} cm^{-3}.

In Fig. 10(c), while changing the absorber layer thickness from 400 to 1200 nm and N_t from 10^{14} to $\leq 10^{18}$ cm^{-3}, the SnS$_2$ ETL consistently maintained a V_{OC} value above 0.936 V across varied thicknesses and defect densities. The same pattern is observed for IGZO, WS$_2$, and ZnO in Fig. 10(d–f). The lowest peak value of V_{OC} shown for PCBM and LBSO ETLs were shown in Fig. 10(a and b). The J_{SC} value decreased with increasing defect density and absorber thickness.

The 3D plots in Fig. 11(a–f) depict how the thickness of the absorber layer and defect density affect the J_{SC} of the solar cells with LBSO, SnS$_2$, IGZO, WS$_2$, and ZnO ETLs. Among all ETLs, an increase in the defect density generally results in a drop in J_{SC}, as seen by the shift from blue or green regions (higher J_{SC}) to yellow or red regions (lower J_{SC}). In contrast, increasing the absorber thickness typically resulted in an improvement in the J_{SC} performance, with the best values observed at a thickness of 500 nm. WS$_2$ and ZnO (Fig. 11(e and f)) exhibit a high potential

J_{SC} of up to 30.917 mA cm^{-2} and 30.878 mA cm^{-2}, respectively, which is attributed to their lower defect density ($<10^{16}$ cm^{-3}) and thicker layers. While SnS$_2$ (Fig. 11c), IGZO (Fig. 11d), and WS$_2$ (Fig. 11e) show similar trends, their peak J_{SC} values are slightly lower. The lowest peak value of J_{SC} is shown for PCBM and LBSO ETLs in Fig. 11(a and b).

Fig. 12(a–f) shows the effect of the absorber layer thickness and defect density on the FF of solar cells using various ETLs such as PCBM, LBSO, SnS$_2$, IGZO, WS$_2$, and ZnO. An increase in the defect density generally results in a decrease in FF, as seen by the transition from blue/green regions (higher FF) to yellow/red regions (lower FF) with increasing defect density. The connection between the absorber layer thickness and FF is more complicated, with thicker absorber layers in Fig. 12(c–f) showing a modest enhancement in FF and the highest FF value of around 87%. The lowest peak value of FF is shown for the PCBM and LBSO ETLs in Fig. 12(a and b).

Finally, the 3D plots in Fig. 13(a–d) illustrate how varying the absorber layer thickness and defect density affects the PCE of
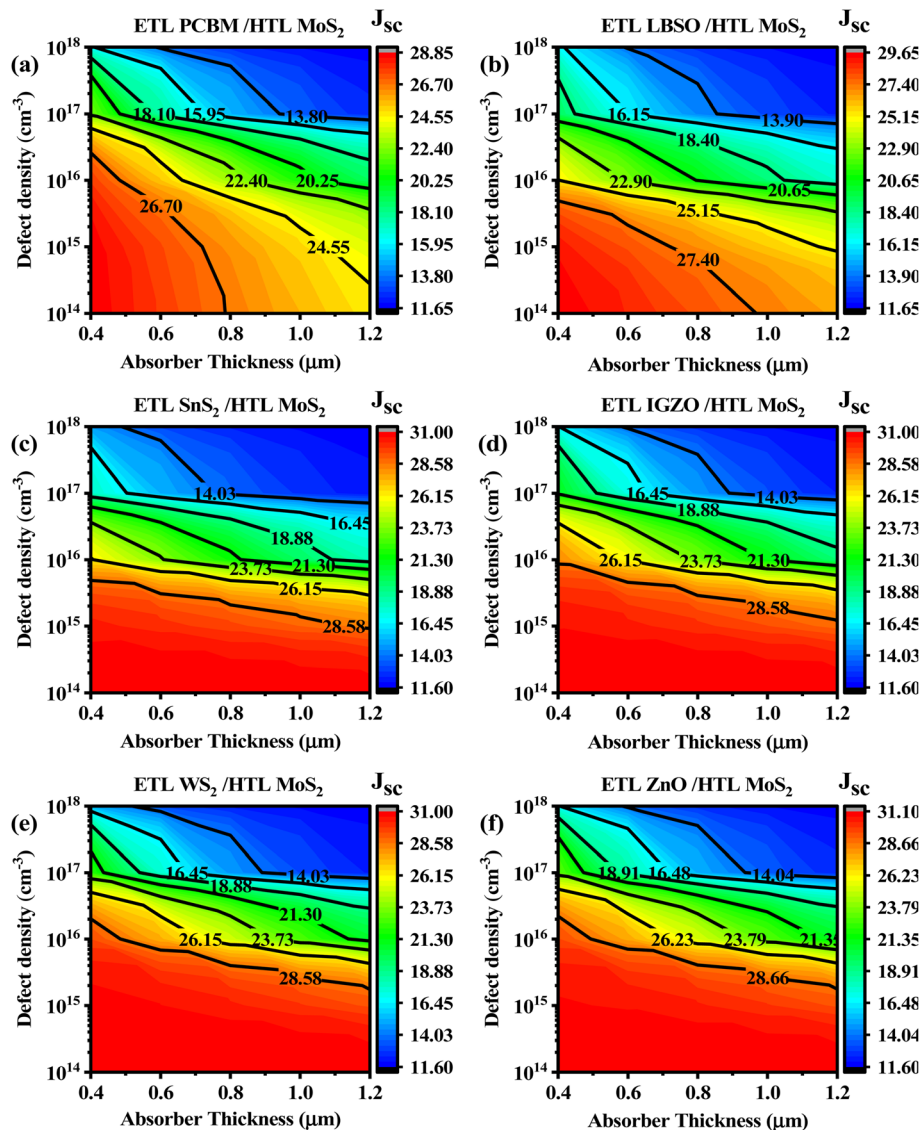
Fig. 11 Contour map of J_{SC} dependency on absorber defect density and thickness when ETL is (a) PCBM, (b) LBSO, (c) SnS$_2$, (d) IGZO, (e) WS$_2$, and (f) ZnO.

solar cells utilizing various ETLs such as PCBM, LBSO, SnS$_2$, IGZO, WS$_2$, and ZnO. There is a direct link between the PCE, thicker absorber layers, and lower defect densities across all ETLs. At an absorber thickness of 500 nm and the defect density of $<10^{16}$ cm^{-3}, IGZO, WS$_2$, and ZnO ETLs in Fig. 13(d–f) demonstrate the highest PCE of around 25.2%. The lowest peak value of the PCE is shown for the PCBM and LBSO ETLs in Fig. 13(a and b).

The defect densities in this case were below 10^{15} cm^{-3}, hence there was no substantial difference in efficiency. Regardless, the defect density increases and the efficiency decreases regardless of the absorber thickness, showing that once the defect density reaches a certain level, the thickness of the absorber layer becomes irrelevant to the performance. Increased carrier recombination, which correlates to an increased N_t in the perovskite layer, speeds up the recombination of photo-generated carriers. V_{OC} can be expressed as follows using eqn (14).

$$V_{OC} = \frac{kT}{e} \ln\left[1 + \frac{J_{SC}}{J_0}\right] \quad (14)$$

Here, k denotes the Boltzmann constant, T is the operating temperature, J_{SC} is the short-circuit current density, J_0 is the reverse saturation current, and e is the electron charge.[67,68]

Furthermore, J_0 increases when the diffusion length, J_{SC}, and V_{OC} decrease, resulting in lower PCE.[69,70] As N_t increases in solar cells, carriers find it more challenging to move through the material.[70] The overall performance of the device is degraded because of the reduced band bending in the absorber layer caused by this increased defect density, which decreases the V_{OC} and produces a smaller effective barrier.[58,71] A higher defect density also accelerates recombination rates, which lowers the CB's charge carrier number. This ultimately results in decreased PCE, FF, J_{SC}, and V_{OC}.[72]

Effects of different absorber types and fault densities on solar cell performance. Defects in the manufacturing process
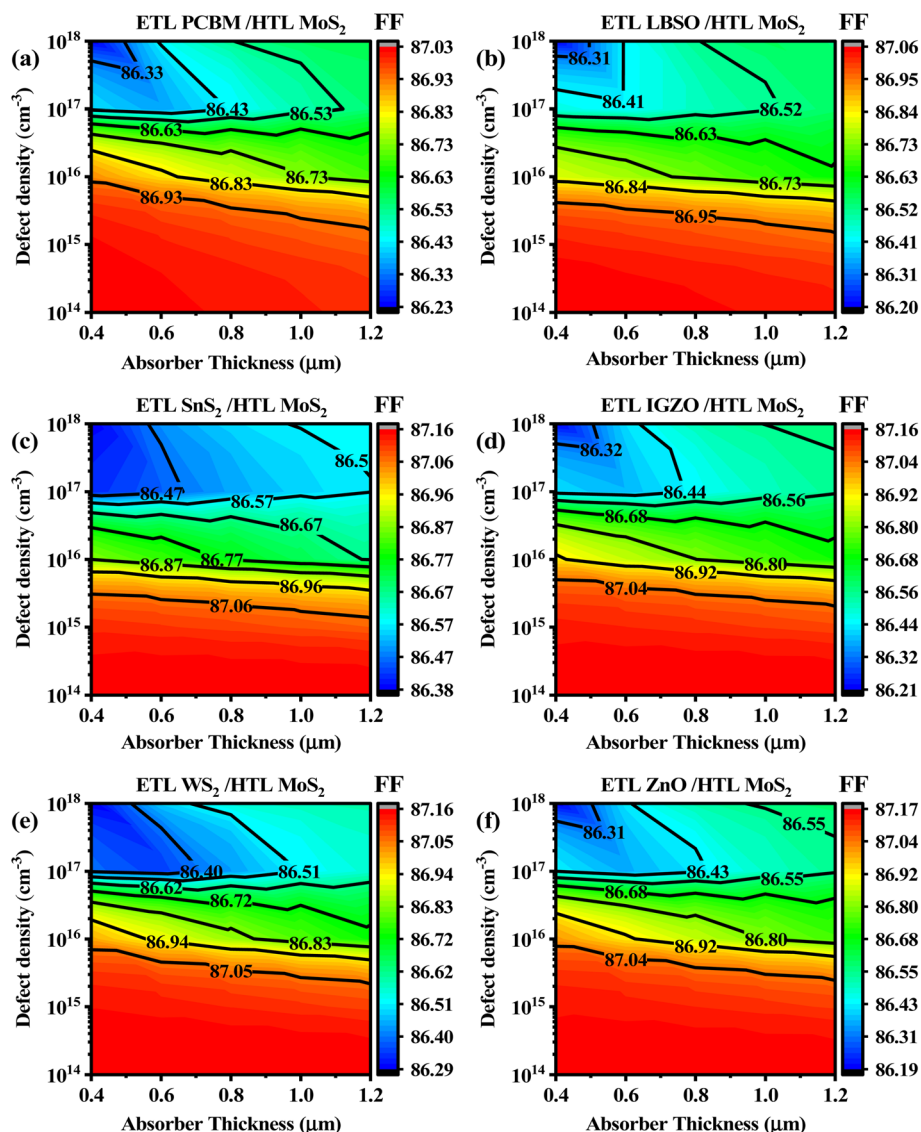
Fig. 12 Contour map of FF dependency on absorber defect density and thickness when ETL is (a) PCBM, (b) LBSO, (c) SnS$_2$, (d) IGZO, (e) WS$_2$, and (f) ZnO.

can significantly affect the optoelectrical characteristics of a material. Examining the association between the defect density in the absorber layer and the thickness of the absorber layer is important because flaws inside the absorption layer of photovoltaic cells can negatively affect their performance. In our simulation, we incorporated a singular deep-level defect state exhibiting donor-like characteristics, attributed to its comparatively lower formation energy relative to that of conventional donors.[73] Throughout the simulation, the absorber layer thickness and defect density were adjusted from 400 to 1200 nm and 10^{14} to 10^{18} cm^{-3}, respectively, to examine the influence on sunlight harvesting characteristics of the six optimized PSCs (Fig. 10–13).

Moreover, the defect density has a substantial impact on the PCE. Higher defect densities cause a significant decline in the PCE, with a shift from blue/green (greater PCE) to yellow/red (lower PCE). When the defect densities exceeded 10^{16}

cm^{-3}, the PCE values declined significantly and demonstrated a smoother decline in PCE as the density increased. To obtain the optimum PCE, it is essential to maintain low defect densities and to use thicker absorber layers, as demonstrated in the plots. SnS$_2$, IGZO, WS$_2$, and ZnO ETLs-based PSCs have been found to have the highest potential efficiencies, around 25.2%. These ETLs have demonstrated outstanding resilience to variation of absorber (CsCdI$_3$) thickness and defect density, making them the best options for optimizing solar cell performance.

3.3. Optimization of the thickness of absorber and HTL by observing effects on PV performance parameters

3.3.1. Impact of absorber layer thickness. To improve solar cell performance, the thickness of the absorber layer must be optimized. Charge carriers tend to recombine when the absorber layer is larger than the diffusion width. Because it
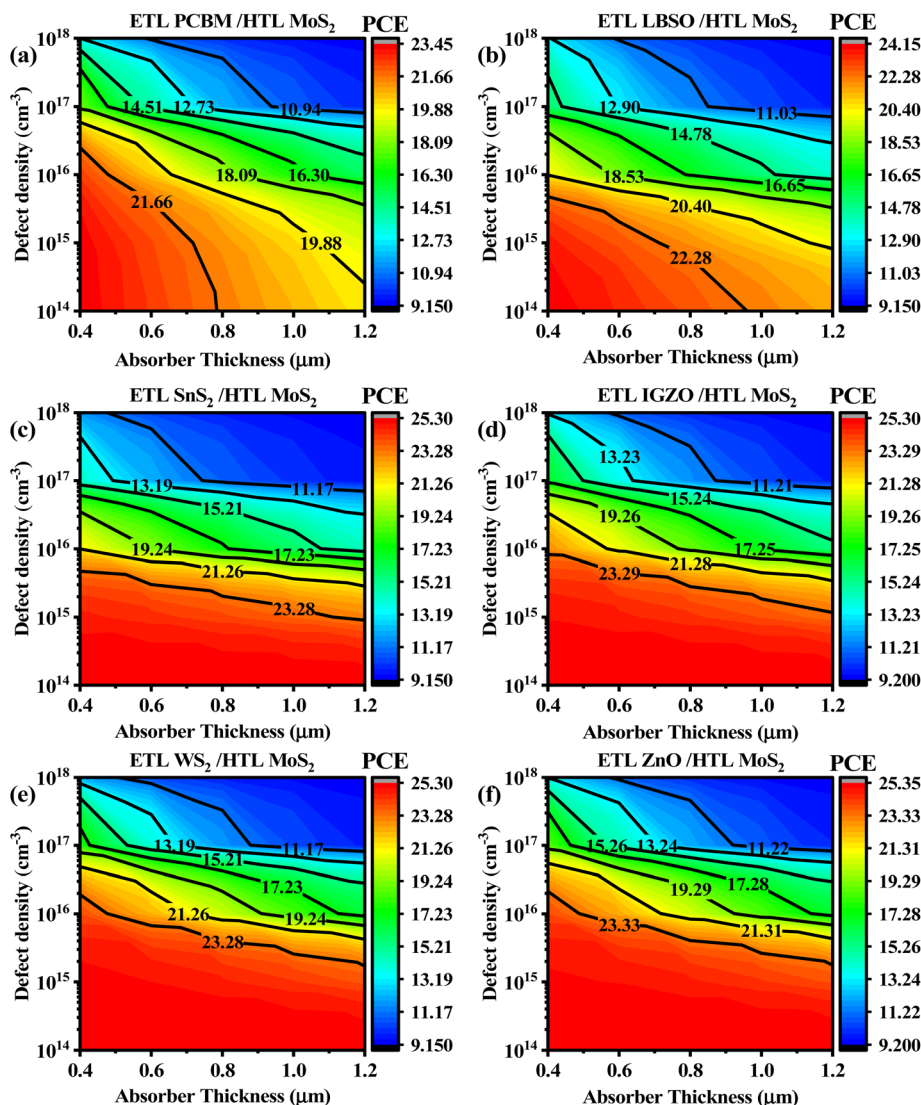
Fig. 13 Contour map of PCE dependency on absorber defect density and thickness when ETL is (a) PCBM, (b) LBSO, (c) SnS$_2$, (d) IGZO, (e) WS$_2$, and (f) ZnO.

increases series resistance and prevents charges from reaching the electrode, this results in a poor PCE. On the other hand, light absorption decreases with an excessively thin absorber layer, which lowers the photocurrent.[74]

Thus, optimizing solar cell performance requires determining the optimal absorber layer thickness. Because this parameter greatly impacts the behavior of the ITO/ZnO/CsCdI$_3$/MoS$_2$/Ni structure, we investigated how changing the absorber thickness from 400 to 1200 nm affects the device performance. The relationship between the PSC performance and variations in the absorber thickness when combined with the ZnO ETL and MoS$_2$ is shown in Fig. 14(a). During the optimization procedure, when the thickness of the absorber and the reverse saturation current increased, the V_{OC} of the solar cell decreased.[75] This structure, associated with the ZnO-based ETL and MoS$_2$-based HTL, exhibited the highest V_{OC} of almost 0.9362 V at approximately 500 nm, demonstrating that as absorber thickness increased, an almost negligible decrease

was observed. The absorber thickness in this design decreased steadily from 0.9362 to 0.9349 V.

The absorber thickness for J_{SC} ranged from 30.7447 to 29.3897 mA cm^{-2}, exhibiting a nearly exponential decreasing pattern over time. This structure, associated with the ZnO ETL, and MoS$_2$ HTL, exhibited the highest J_{SC} of almost 30.7447 mA cm^{-2}, approximately at 500 nm, indicating similar behavior. In addition, as the absorber thickness increased, an almost linear decline was observed.

The FF for this structure associated with the ZnO-based ETL and MoS$_2$-based HTL exhibited a nearly exponential decreasing pattern with the increase in absorber thickness, which is the same behavior as the J_{SC}. This configuration showed a steady drop with the absorber thickness ranging from 87.1396–87.0995% and exhibited the highest FF of 87.11862% at approximately 500 nm.

With regard to the PCE, a declining trend that was similar to that of the FF and J_{SC} mentioned above was observed with an
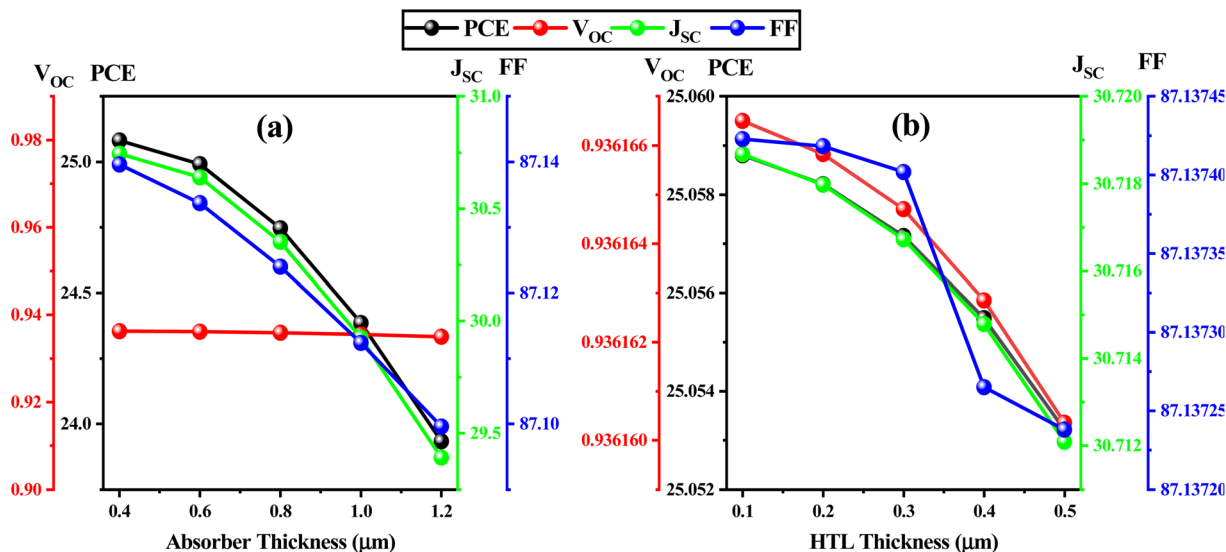
Fig. 14 Influence on PV parameters considering the variation in (a) absorber ($CsCdI_3$) thickness, and (b) HTL (MoS_2) thickness.

increase in absorber thickness. This shows a nearly exponential decreasing pattern with absorber thickness from 25.0813 to 23.9322%. In addition, it exhibited the highest PCE of 25.0813% at approximately 500 nm.

3.3.2. Impact of HTL layer thickness. Fig. 14(b) illustrates how changing the thickness of the MoS_2-based HTL affects the key performance parameters in $CsCdI_3$-based PSCs that use ZnO as the ETL. Because MoS_2 showed the highest PCE in earlier testing, it was chosen as the HTL for thickness optimization.

We increased the HTL thickness from 100 to 500 nm to evaluate its effect on the performance of the ITO/ZnO/$CsCdI_3$/MoS_2/Ni structure. Fig. 14(b) shows that most PSC parameters follow a similar pattern with increasing HTL thickness. The data revealed an almost linear decrease in the overall performance as the HTL thickness increased when paired with the ZnO ETL. The highest V_{OC} value of 0.936167 V was observed at a minimum HTL thickness of 100 nm, whereas the lowest was 0.93616 V at 500 nm. It showed a nearly exponential decreasing trend.

With an increase in HTL thickness, J_{SC} exhibited an almost exponential declining trend, going from 30.7187 to 30.7121 mA cm^{-2}. The highest J_{SC} value, 30.7187 mA cm^{-2}, is measured at 100 nm, whereas the lowest, 30.7121 mA cm^{-2}, is measured at the same thickness.

As the HTL thickness increased, the FF for this structure associated with the ZnO ETL exhibited a small decline pattern, which was similar to the trend observed for V_{OC}. As the HTL thickness increases, this configuration showed a consistent decrease, ranging from 87.137423 to 87.137238%, and exhibited the highest FF of 87.137423% at 100 nm.

In the context of the PCE, as the HTL thickness increased, it displayed a nearly exponential decreasing pattern. At 100 nm, the maximum value was 25.0588%, whereas the lowest value was 25.0532% observed at 500 nm. A prior investigation demonstrated that increasing the HTL thickness improved

efficiency.[76] The HTL thickness is an important component for maximizing the device performance. Optimal performance can be achieved by selecting a thickness that maximizes light emission and charge transfer within a particular range.

The above 3.3 analysis suggests that the optimal thickness of the absorber for enhancing PSC parameters is 500 nm. And the optimal HTL thickness is 200 nm, which is consistent with the previous study.[47]

3.4. Influences of various parameters on the PV parameters

3.4.1. Effect of series resistance. The efficiency of solar cells is significantly affected by the existence of shunt (R_{sh}) and series (R_s) resistances, mostly owing to connections between the cell layers, manufacturing flaws, and metal contacts that surround the cell's sidewalls.[14] For six single-halide perovskite devices with six ETLs (ITO/ETLs/$CsCdI_3$/MoS_2/Ni), R_{sh} remained constant at 10^5 Ω cm^2, while the effect of R_s changed from 0 to 6 Ω cm^2 as shown in Fig. 15. In Fig. 15(d), when R_s variation occurs, the PCE decreases for all six $CsCdI_3$ perovskite device designs. In the ZnO ETL-based $CsCdI_3$ perovskite device structure, the highest PCE was 25.0518%, and the PCE values dropped roughly to 19.8611% as R_s increased. On the contrary, as R_s increased in the PCBM ETL-based $CsCdI_3$ perovskite device structure, the lowest PCE was 22.8154%, and the PCE values dropped by approximately 18.4818%. The ZnO ETL-based $CsCdI_3$ perovskite device structure shows an abrupt drop as the R_s increases. In Fig. 15(c), the FF value, however, was larger for every solar cell connected to the ETL, and it decreased as R_s increased. In Fig. 15(b), the J_{SC} saw a little drop in all ETL-based configurations as R_s increased.

The ZnO ETL-based configuration experienced the highest J_{SC} value and dropped from 30.7189 to 30.7131 mA cm^{-2}, and the PCBM ETL-based structure experienced the lowest J_{SC} value and dropped from 28.0951 to 28.0835 mA cm^{-2}. As R_s increased for all ETL-based devices, the PCE, FF, and J_{SC}
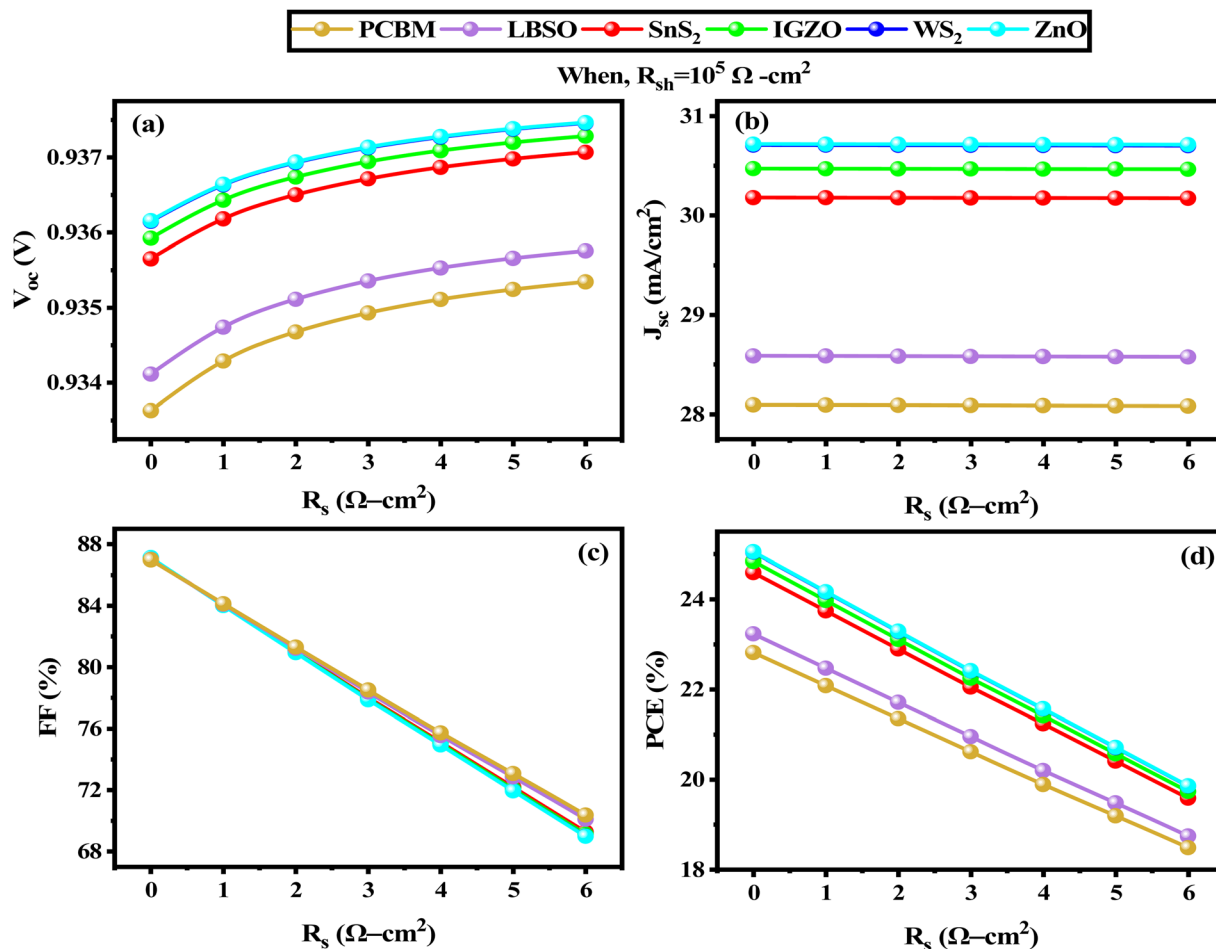
Fig. 15 Influence of variation in series resistance on (a) V_{OC}, (b) J_{SC}, (c) FF, and (d) PCE.

decreased while the V_{OC} performance improved, as illustrated in Fig. 15(a). For the ZnO ETL-associated structure, which experienced the highest V_{OC} value, it increased from 0.9362 to 0.9375 V. For the PCBM ETL-associated structure, which experienced the highest V_{OC} values, it increased from 0.9336 to 0.9353 V. However, changes in R_s had little effect on the J_{SC} and V_{OC} characteristics for all explored device architectures due to the slight fluctuation, which is consistent with the previous work.[14] For these specific devices, the currents with $R_s \geq 30\ \Omega$ cm^2 tended to decrease beyond this range, leading to a slight reduction.[77] R_s is the total resistance between the absorber, HTL, and ETL, and the solar cell's FMC and BMC, of the solar cell, which have no influence on the current. Consequently, characteristics such as consistency, R_s, and R_{sh} together result in decreased efficiency, especially with larger modules and PSC's areas.[78–80]

3.4.2. Effect of shunt resistance. In photovoltaic solar cells, an important internal electrical parameter known as R_{sh} plays a crucial role in determining the overall efficiency. This resistance parameter governs leakage currents occurring at the interfaces where the active layer meets the electrodes, as well as at the junctions between the donor and acceptor materials.[31] For PSCs, R_{sh} issues stem primarily from two sources: physical

defects such as pinholes in the photoactive layer that create leakage pathways, and various recombination losses. Whereas, R_s originates from several factors, including internal resistances, interface barrier effects, the properties of charge-collecting interlayer materials, and the characteristics of the metal-based electrodes themselves.[81] The Shockley equation, represented by eqn (15) and (16) describes the predicted behavior of a solar cell's $J–V$ characteristics under ideal one-sun illumination conditions.[82]

$$J_{SC} = J_{PH} - J_0 \left[\exp\left(\frac{q_e(V - JR_s)}{nkT_e}\right)\right] - \frac{V - JR_s}{R_{sh}} \quad (15)$$

$$V_{OC} = \left(\frac{nkT_e}{q_e}\right)\ln\left\{\frac{J_{PH}}{J_0}\left(1 - \frac{V_{OC}}{J_{PH}R_{sh}}\right)\right\} \quad (16)$$

where q_e is the elementary charge, J_{PH} represents the photocurrent density, J_0 is the density of the reverse bias saturation current, R_s refers to the series resistance, R_{sh} is the shunt resistance, n is the diode ideality factor, k is the Boltzmann constant (1.38×1023 J K^{-1}), and T_e denotes the ambient temperature (298 K). Also, eqn (15) and (16) demonstrate that J_{SC} and V_{OC} have a negative inverse relationship with R_{sh}. This means that as R_{sh} increases, so does the J_{SC} and V_{OC}.
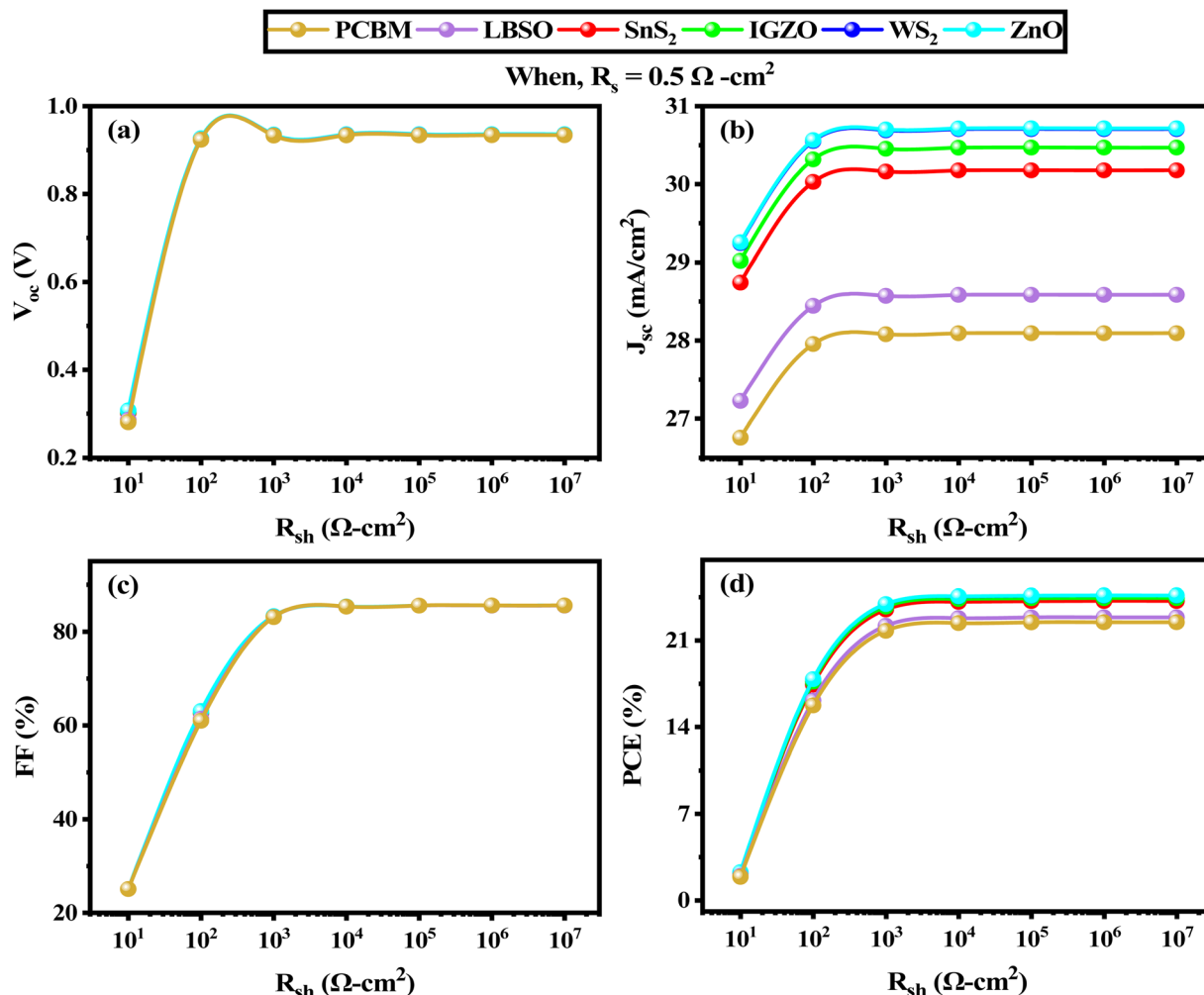
Fig. 16 Influence of variation in shunt resistance on (a) V_{OC}, (b) J_{SC}, (c) FF, and (d) PCE.

In this study, we explored the effect of R_{sh} on six different solar cell configurations, as shown in Fig. 16. In all configurations, R_{sh} was adjusted from 10^1 to 10^7 Ω cm^2 when maintaining a constant R_s of 0.5 Ω cm^2, revealing that photovoltaic performance parameters improved as R_{sh} increased, consistent with findings from prior research.[83] Notably, the V_{OC} and J_{SC} values showed substantial improvement in the lower R_{sh} range from 10^1–10^2 Ω cm^2, when the PCE and FF improved across a wider range of 10^1–10^3 Ω cm^2, after which all parameters stabilized. Specifically in Fig. 16(a), V_{OC} reached its maximum value of approximately 0.93561 V at an R_{sh} value of approximately 10^3 Ω cm^2 and remained steady thereafter. Likewise, in Fig. 16(b), J_{SC} increased between 10^1–10^2 Ω cm^2 R_{sh} range across all configurations before stabilizing. Among the six tested configurations, the ITO/ZnO/CsCdI$_3$/MoS$_2$/Ni PSC achieved the highest J_{SC} of approximately 30.56572 mA cm^{-2}, whereas the ITO/PCBM/CsCdI$_3$/MoS$_2$/Ni PSC configuration produced the lowest J_{SC} of approximately 27.95454 mA cm^{-2}. Regarding FF in Fig. 16(c), ITO/ZnO/CsCdI$_3$/MoS$_2$/Ni PSC reached the highest FF of approximately 83.30486%, whereas ITO/PCBM/CsCdI$_3$/MoS$_2$/Ni showed the lowest FF of approximately 83.08378%. All

configurations responded similarly to the changes in R_{sh}. In terms of overall performance, the ITO/ZnO/CsCdI$_3$/MoS$_2$/Ni configuration achieved the highest PCE of approximately 23.93035%, whereas ITO/PCBM/CsCdI$_3$/MoS$_2$/Ni demonstrated the lowest PCE of 21.76960% as illustrated in Fig. 16(d). The changes in several PV parameters when R_{sh} was varied were in line with earlier studies.[84]

3.4.3. Effect of temperature. To assess the stability of the solar cell performance, a comprehensive understanding of solar cell performance at high operating temperatures is crucial. With rising temperatures, many solar cell configurations experience functional instability owing to interfacial distortion between layers. However, recent studies have shown improved stability performance in perovskite-based optoelectronic devices.[85,86] As shown in Fig. 17, the effect of temperature on the six PSC designs was investigated.

The temperatures varied from 270 K to 470 K to understand the connection between temperature and solar cell efficiency. The photovoltaic parameters across all six configurations demonstrated significant temperature dependence. Fig. 17(b) reveals that J_{SC} increased with temperature for nearly all ideal
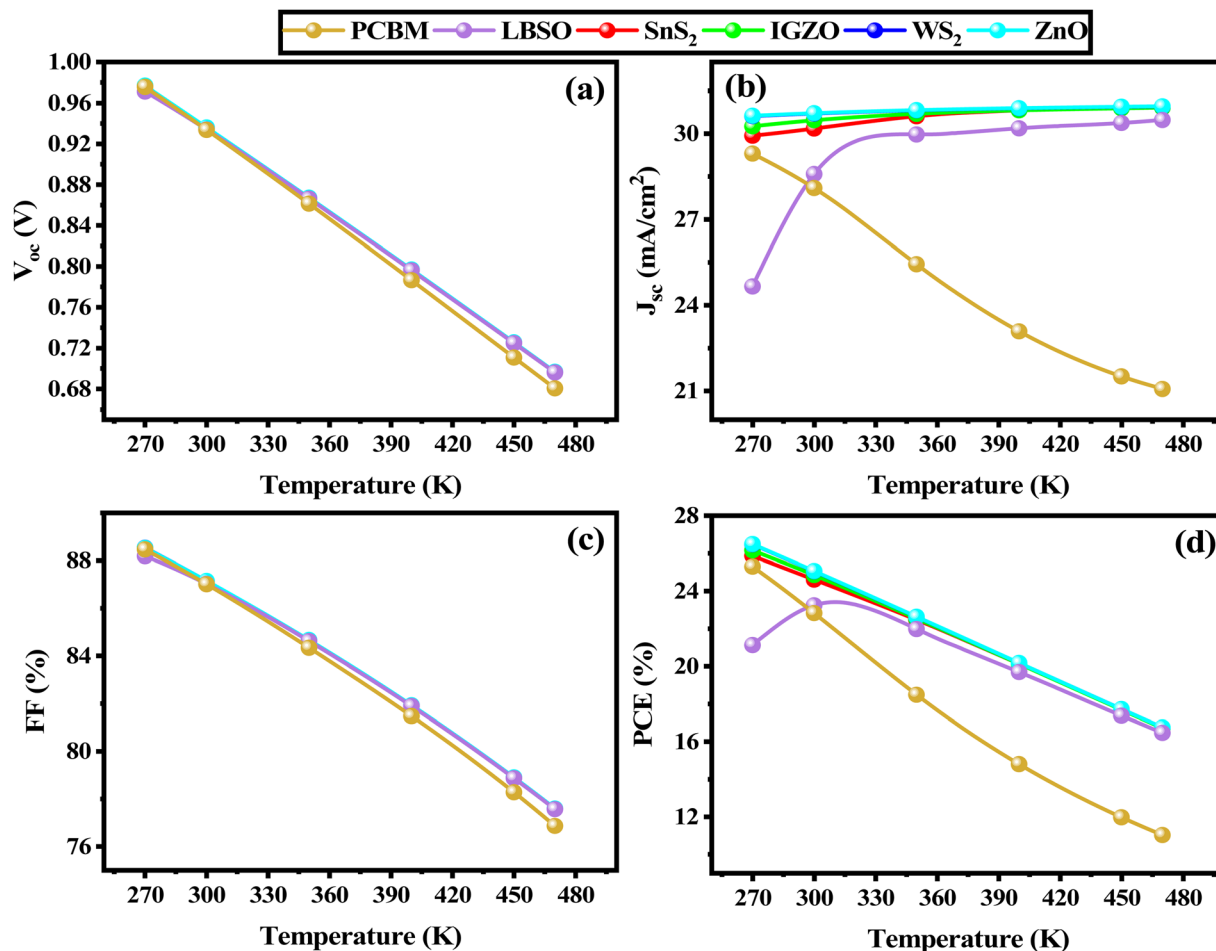
Fig. 17 Influence of variation in temperature on (a) V_{OC}, (b) J_{SC}, (c) FF, and (d) PCE.

solar cell structures, with the notable exception of the PCBM-based ETL devices. This distinctive temperature response behavior of PCBM-based ETLs differed markedly from the temperature response patterns observed in the other ETL configurations. In contrast, J_{SC} increased marginally for SnS$_2$, IGZO, WS$_2$, and ZnO ETLs-based PSC devices, and the LBSO ETL-based PSC setup roughly increased as the temperature increased, whereas the PCBM ETL-based PSC setup roughly decreased as the temperature increased.

In Fig. 17(d), the ITO/ZnO/CsCdI$_3$/MoS$_2$/Ni PSC exhibited the highest efficiency (PCE) of approximately 26.48666% at 270 K, which dropped to 16.73522% as the temperature increased which is consistent with the previous study,[32] while the ITO/PCBM/CsCdI$_3$/MoS$_2$/Ni PSC dropped to 11.01699% at 470 K temperature. However, ITO/LBSO/CsCdI$_3$/MoS$_2$/Ni exhibited different responses in comparison with other ETL responses with variations in temperature. It first increased from 21.12127 to 23.23776% at 300 K, then decreased and fell to 16.45326%. The ITO/WS$_2$/CsCdI$_3$/MoS$_2$/Ni PSC showed the highest FF of around 88.52340% at 270 K temperature and dropped to 77.58527% with increasing temperature, while the ITO/PCBM/CsCdI$_3$/MoS$_2$/Ni PSC dropped to 76.85759% at 470 K temperature, as illustrated in Fig. 17(c). A similar trend was observed for

the other four PSCs; the FF decreased as the temperature increased. Interestingly, the J_{SC}'s response to variations in temperature is the opposite of the PCE's variation, with the exception of PCBM. This means that with an increase in temperature, the J_{SC} of all ETLs except PCBM increased, whereas in PCE, they decreased. PCBM showed an exact response similar to that of PCE. When examining the temperature effects as the temperature increased, all six solar cell structures exhibited a consistent pattern of decreasing V_{OC}. The V_{OC} values decreased from around 0.97692 V to around 0.69669 V across most of the ETLs, with PCBM-based ETL showing the most pronounced reduction, dropping to a minimum value of 0.68045 V. The inverse connection between V_{OC} and J_0, which results in a fall in V_{OC} values across all high-efficiency device designs as temperatures rise, is responsible for this uniform decrease in V_{OC} with increasing temperatures. At higher temperatures, J_0 increased. The below eqn (17) shows the relationship between V_{OC} and J_0.

$$V_{OC} = \frac{AKT_1}{q}\left[\ln\left(\frac{J_{SC}}{J_0} + 1\right)\right] \quad (17)$$

Subsequently, defects increase as the PSC's temperature increases, resulting in a decrease in V_{OC}, aligns with the

previous research.[14] The current experienced only slight changes owing to bandgap narrowing as the temperature increased. However, this variation was minimal and appeared to stabilize at higher temperatures. Additionally, as the temperature increases, both the diffusion length and R_s undergo changes that directly affect the FF and PCE of the device.[60,87]

3.4.4. Influence of the capacitance and MS. Fig. 18(a and b) displays the six solar cells' M–S and capacitance per unit area (C) graphs with the bias voltage (V). The well-established M–S analytical method enables calculation from capacitance–voltage (C–V) measurements of both the charge carrier density (N_d) and built-in voltage (V_{bi}). This experimental approach has gained widespread adoption in traditional semiconductor devices, particularly at p–n junctions and semiconductor–metal interfaces, where it effectively characterizes fixed depletion layers and space charge regions. The junction capacitance per unit area (C) can be quantitatively determined using eqn (18).

$$\frac{1}{C^2} = \frac{2\varepsilon_0\varepsilon_r}{qN_d}(V_{bi} - V) \tag{18}$$

Here, q represents the electronic charge, ε_r indicates the dielectric constant of the donor, ε_0 refers to vacuum permittivity, and V denotes the applied voltage, as shown in Fig. 18(b).[88] The carrier concentration N is obtained from the

linear portion's slope, whereas V_{bi} can be determined by extending this linear segment to intersect with the voltage axis. Throughout the measurements, the frequency was maintained at a constant 1 MHz, with voltage variations ranging from −0.8 V to 0.8 V, as illustrated in Fig. 18. The Fig. 18(a) demonstrates that the capacitance for all six optimized devices increases exponentially as V increases. Each solar cell structure with different ETLs showed a dramatic exponential increase when reaching 0.8 V. The ITO/LBSO/CsCdI$_3$/MoS$_2$/Ni configuration achieved the highest capacitance value of approximately 207.65481C. This was closely followed by PCBM, SnS$_2$, IGZO, and ZnO-based structures, which displayed capacitance values of approximately 207.36705C, 207.36019C, 207.35957C, and 207.35917C, respectively, and the ITO/WS$_2$/CsCdI$_3$/MoS$_2$/Ni exhibited the lowest peak capacitance value of approximately 207.35128C. Although there are slight changes among the ETLs in Fig. 18(a), it seems that they overlap with one another. The current stays much below saturation levels when running at low voltages, only reaching full saturation when the contact points experience voltage surges.[89] As a result, the capacitance varied with the applied voltage, demonstrating its suitability for voltage-controlled solar cell applications.

Meanwhile, to determine built-in potential (V_{bi}) of a device, which measures the effectiveness difference between the doping level and the electrode, researchers commonly employ
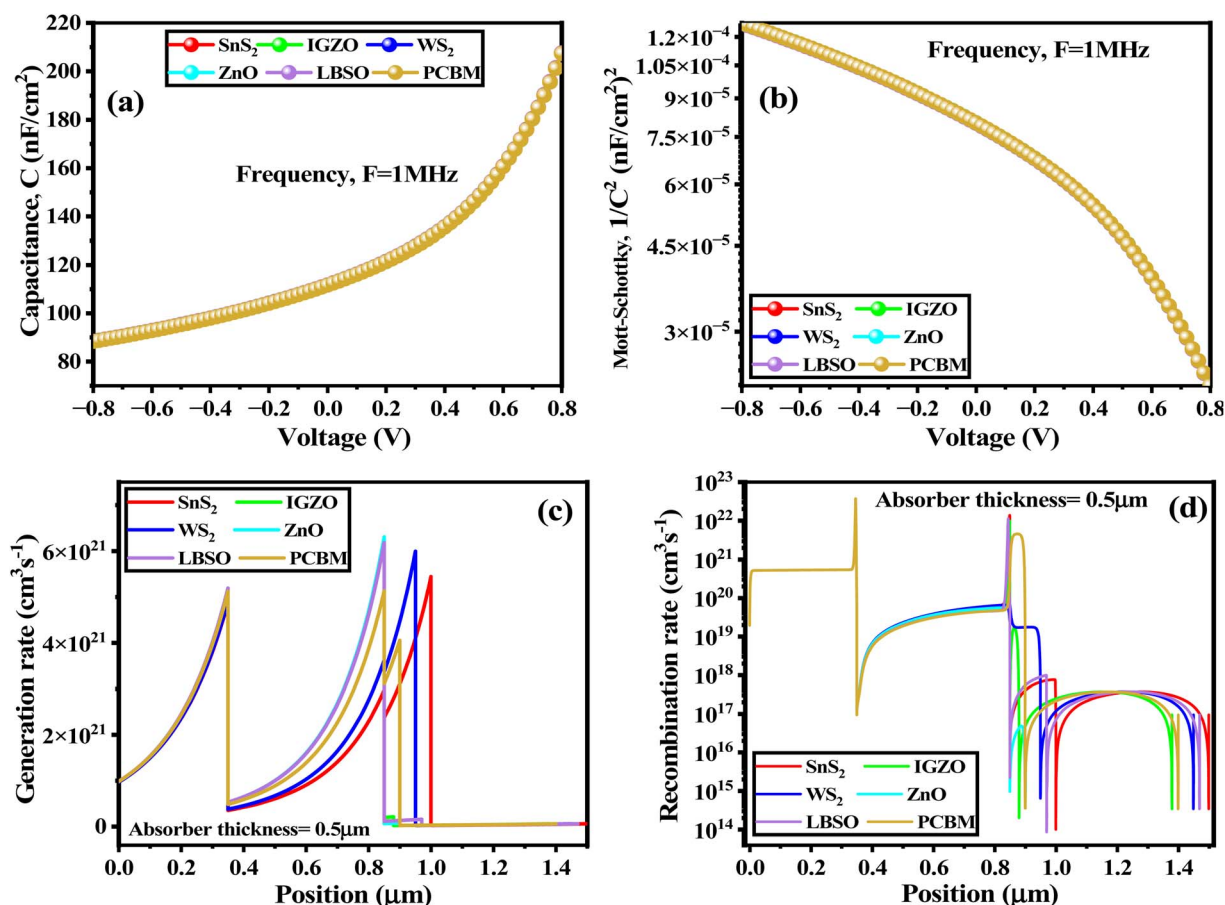

Fig. 18 (a) Capacitance, (b) MS plot, (c) generation rate, and (d) recombination rate for the CsCdI$_3$ perovskite solar cell.

MS analysis.[79] This widely respected analytical technique has established itself as a reliable method for identifying built-in potential values in such devices.[90] In our analysis, Fig. 18(b) shows an opposite pattern. In this case, as the voltage range changed from −0.8 to 0.8 V, all six PSCs showed an exponential decrease. When comparing various perovskite solar cell configurations, our findings revealed notable differences in MS values. The $ITO/ZnO/CsCdI_3/MoS_2/Ni$ and $ITO/WS_2/CsCdI_3/MoS_2/Ni$ structures displayed superior performance, with the highest Mott–Schottky measurements at around 2.32588×10^{-5} $1/C^2$. In contrast, the $ITO/LBSO/CsCdI_3/MoS_2/Ni$ configuration showed the most modest results, with measurements reaching only approximately 2.31908×10^{-5} $1/C^2$. Although there are slight changes among the ETLs as shown in Fig. 18(b), it seems that they overlap with one another. As seen in Fig. 18(b), as the applied voltage rises, the Mott–Schottky graph shows a decrease, which is in accordance with previous observations.[91]

3.4.5. Influence of the generation and recombination rate. The generation and recombination rates for the six different configurations for the six different ETLs are shown in Fig. 18(c and d). As electrons move from the valence band to the conduction band during carrier development, holes are left in the valence band, forming electron–hole pairs.[13] As shown in Fig. 18(c), all six device configurations reached their peak generation rates at approximately the 850 nm position. In the SCAPS-1D simulation framework, the photon flux, $N_{phot}(\lambda, x)$, was used to determine the electron–hole pair generation rate, $G(x)$, using the relationship given in eqn (19):

$$G(\lambda, x) = \alpha(\lambda, x)N_{phot}(\lambda, x) \quad (19)$$

In the conduction band, recombination involves the formation and extinction of electrons and holes, in contrast to generation.[83] During this process, the defect states of each layer play a crucial role in creating energy levels that significantly affect the recombination behavior. The interfaces, junctions, and grain boundaries in perovskite solar cells can create uneven recombination rate distributions throughout the device structure.[14] As illustrated in Fig. 18(d), the recombination process begins at relatively modest rates before intensifying. In this figure, the IGZO, SnS_2, and ZnO ETLs-based PSC exhibit nearly the highest recombination rates at 0.34635 μm, 3.65574×10^{22} $cm^3 s^{-1}$, 3.65574×10^{22} $cm^3 s^{-1}$, and 3.65576×10^{22} $cm^3 s^{-1}$. In addition, the $ITO/WS_2/CsCdI_3/MoS_2/Ni$ PSC exhibited the lowest recombination rate at 1.00645 μm, and that is 8.48194×10^{13} $cm^3 s^{-1}$.

3.4.6. J–V and QE characteristics of $CsCdI_3$. Fig. 19(a) shows the variance in the J–V characteristics of the six studied solar cell configurations. The voltage in this instance fell between 0 and 1 V. Up to 0.94 V, the procedure operated consistently for every structure. All the ETL-based PSC's curves show nearly parallel photocurrent waves till 0.82 V. Subsequently, at 0.92 V, it abruptly collapses to zero before reaching 1 V. The $ITO/ZnO/CsCdI_3/MoS_2/Ni$ PSC showed the highest photocurrent value, approximately 30.71887 mA cm^{-2}, whereas the $ITO/PCBM/CsCdI_3/MoS_2/Ni$ PSC exhibited the lowest photocurrent value of approximately 28.09513 mA cm^{-2} at 0 V. On the other hand, the SnS_2, IGZO, WS_2, and LBSO ETL-based device achieved 30.17945 mA cm^{-2}, 30.47107 mA cm^{-2}, 30.7086 mA cm^{-2}, and 28.58713 mA cm^{-2}, respectively. This minor variation reflects differences in band alignment, carrier transport, and optical absorption for each ETL. The Shockley–Queisser's limit of J_{SC} is 35.82 mA cm^{-2}.[92] The performance of these devices is primarily affected by the defect concentrations within the perovskite films, which serve as primary sites for photoelectron generation. Understanding the electron–hole recombination dynamics within the perovskite layer is essential for characterizing the photovoltaic properties of these solar
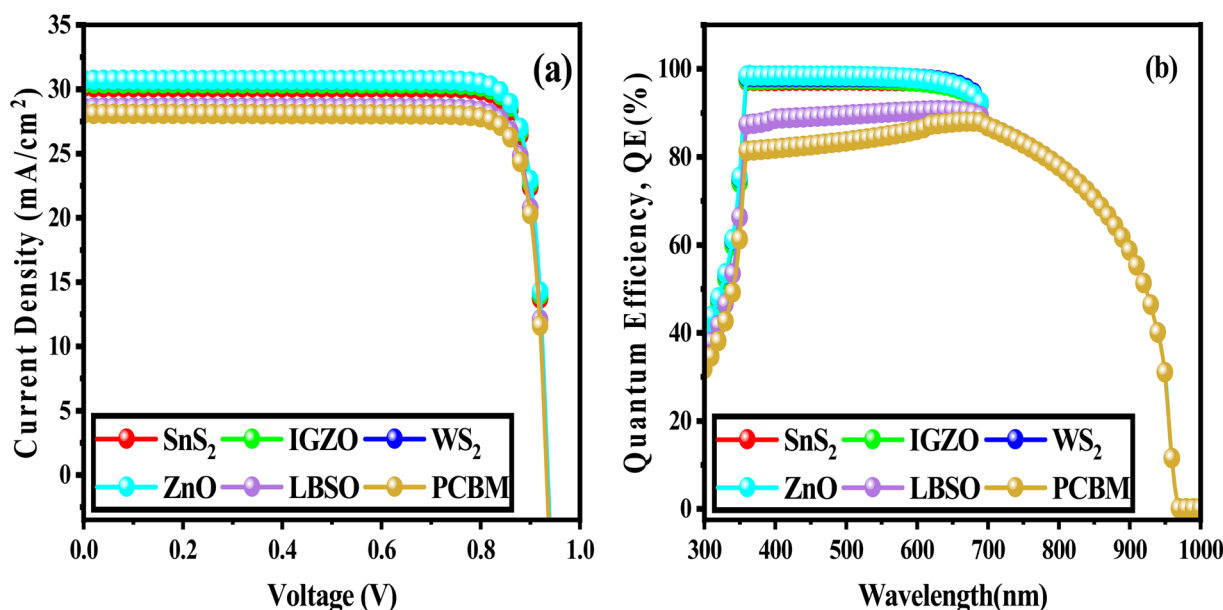

Fig. 19 (a) J–V characteristics and (b) quantum efficiency (QE) curve of $CsCdI_3$ PSC.

cells, as reflected in their current–voltage (J–V) curves. This aligns with observations that the exceptional crystallinity of perovskite materials enhances device functionality while simultaneously reducing charge-carrier recombination.[93]

The QE is the fraction of excited carriers that combine in a radiative manner with total recombination. The QE of a solar cell is dependent on the incident light wavelength (λ). It is defined as the ratio between the number of photogenerated charge carriers and the number of incident photons on the device.[94] Fig. 19(b) shows the QE curve at particular wavelengths between 300 and 1000 nm. Sharp exponential growth was observed for all combinations within the wavelength range of 300–360 nm. Subsequently, between 360 and 670 nm, the SnS_2, IGZO, WS_2, and ZnO ETLs based PSC curves demonstrate nearly constant behavior, illustrating how the QE remains uninfluenced except for the LBSO, and PCBM ETLs based PSCs, whose curves demonstrate slightly increasing behavior until 670 nm. The QE plot (Fig. 19(b)) against the wavelength showed that close to 100% of the wavelength between 360 nm, and 690 nm recombined in a radiative way for SnS_2, IGZO, WS_2, and ZnO ETLs, while close to 90%, and 80% of such wavelengths recombined through other processes, as shown in Fig. 19(b), for both LBSO and PCBM respectively. Beyond 700 nm, the QE of all solar cell devices started to decline and abruptly collapsed to zero before reaching 1 V. As shown in Fig. 19(b), 86% to less than 11% of the wavelength between 700 nm and 960 nm recombines in a radiative manner through every ETL as well. The ITO/ZnO/CsCdI$_3$/MoS$_2$/Ni PSC displayed a slightly higher QE than the other configurations, approximately 99%, whereas the ITO/LBSO/CsCdI$_3$/MoS$_2$/Ni PSC displayed a smaller QE than the other configurations, approximately 81% at 360 nm. A similar trend of QE response in Fig. 19(b) is observed in the previous literature.[32] Recombination processes reduce the QE of most solar cells, thereby preventing charge carriers from flowing into the external circuit. Generally, an increase in absorber layer thickness enhances QE, since a thicker absorber allows the absorption of a larger fraction of incoming photons.[95] Changes to the front surface that alter carriers produced at the interface are among the factors that affect the QE and the collection probability. Additionally, when the forward surface layers contain high doping concentrations, they can cause free carrier absorption, which reduces the QE at longer wavelengths.[96]

3.4.7. Nyquist pot. Impedance analysis is an effective tool for analyzing the behavior of perovskite materials containing various halides.[97] Impedance analysis is one of the most effective approaches for exploring the behavior of perovskite materials with various halides. To further study the influence of all ETLs on V_{OC}, J_{SC}, FF, and PCE obtained from the I–V characteristics, the complex impedance (Z^*) was generated to investigate the impact of ion migration of charge carriers in the perovskite solar cell. Fig. 20 depicts the Nyquist plot of the complex impedance, which displays the development of the imaginary part (Z'') versus the real part (Z') for various ETL materials. The X-axis indicates the resistance owing to recombination, while the Y-axis represents the geometrical capacitance of the solar cell, indicating that carriers accumulate at the interface layers. Each curve shows a nearly single semi-circle
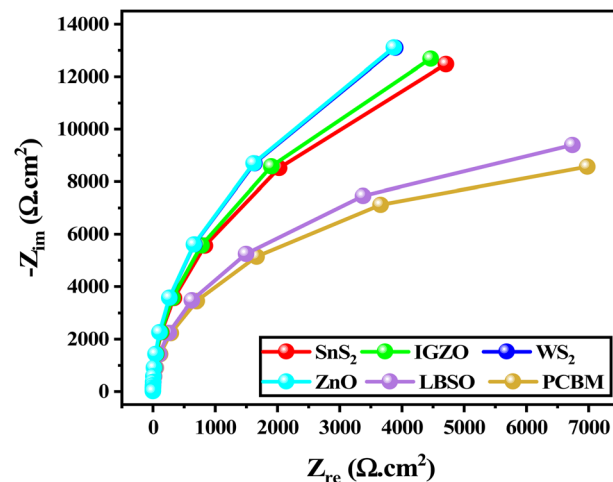

Fig. 20 Nyquist plot of the various ETL materials based on the structure of ITO/ETL/CsCdI$_3$/MoS$_2$/Ni, where PCBM, LBSO, SnS$_2$, IGZO, WS$_2$, and ZnO are used as ETL.

processed within the frequency range of 100–1 MHz. The real (Z_{re}) and imaginary (Z_{im}) components of the impedance are plotted against each other. The impedance spectra for each ETL show only one nearly semi-circle. Furthermore, the width of the nearly semi-circle varies among the different ETL-based structures, indicating varied electrical characteristics and performance consequences. Moreover, the diameter of this nearly semi-circle increases as the frequency increases. Specifically, the wider semicircle associated with the ZnO ETL-based PSC indicates greater impedance or resistance within the system at approximately 13 114.0118 ohm cm^2, which might be related to slowed charge transport kinetics or increased charge transfer resistance at the perovskite-ZnO interface. In contrast, the smaller semi-circle seen for the PCBM ETL-based structure implies a lower impedance of approximately 8560.356 ohm cm^2, which means smoother charge transport, enhanced interface properties, or higher charge carrier mobility than other ETL materials. At high frequencies, the measured resistance is consistent with the recombination resistance of the material. The capacitance at these frequencies corresponds to geometric capacitance, which indicates charge accumulation at the interfaces.[98] The low-frequency response was more baffling, indicating ionic mobility and hysteresis.[99] As ions accumulate and the reduction barriers decrease, this response becomes inductive. The impedance plot of the solar cell, also known as the Nyquist plot, provides a complete qualitative understanding of the device's capacitance, resistive losses, and rate of recombination defects inside the device.

4. Experimental feasibility and material synthesis considerations

4.1. CsCdI$_3$ perovskite synthesis challenges

The experimental realization of CsCdI$_3$ perovskite solar cells faces several key challenges that must be considered alongside our computational predictions.

4.1.1. Crystal structure stability. $CsCdI_3$ adopts a cubic perovskite structure under ambient conditions, but stability concerns arise due to the relatively large ionic radius of Cd^{2+} compared to traditional perovskite B-site cations like Pb^{2+}. The Goldschmidt tolerance factor for $CsCdI_3$ ($t \approx 0.916$) suggests marginal structural stability, which may require careful synthesis conditions to maintain the desired perovskite phase.[54]

4.1.2. Synthesis methods. Several approaches have been reported for Cd-based perovskite synthesis: (1) solution processing: low-temperature spin-coating methods using CsI and CdI_2 precursors in polar solvents (DMF/DMSO).[100] However, the hygroscopic nature of cesium iodide and the tendency of cadmium-based perovskites to form secondary phases pose significant challenges. The formation of non-perovskite phases such as Cs_2CdI_4 or $CsCd_2I_5$ can occur under non-optimal synthesis conditions, affecting the optoelectronic properties.[4] Additionally, the toxicity concerns associated with cadmium compounds require careful handling protocols and may limit widespread commercial applications despite the superior stability compared to lead-based alternatives.[5] (2) Vapor deposition: sequential thermal evaporation of constituent materials, though requiring precise temperature control due to CdI_2 volatility[101] This technique involves exposing a solution-processed precursor film to organic halide vapors, promoting crystallization and grain growth. For $CsCdI_3$, optimization of annealing temperatures (typically 150–200 °C) and controlled atmosphere conditions are crucial for achieving phase-pure materials.[7] And (3) hot-injection method: colloidal synthesis for nanocrystal formation, offering better size control but requiring surface ligand management.[102]

4.1.3. Environmental and toxicity concerns. Unlike lead-based perovskites, cadmium-based materials face significant regulatory challenges due to Cd toxicity. This necessitates careful handling protocols and may limit commercial viability despite superior optoelectronic properties predicted in our simulations.[103]

4.2. Device fabrication challenges

4.2.1. Interface engineering. Our simulations assume ideal interfaces, but experimental devices require careful optimization of: (1) electron transport layer (ETL) alignment: SnS_2, PCBM, IGZO, LBSO, WS_2, or ZnO with appropriate surface treatments[10] (2) hole transport layer (HTL) selection: MoS_2, Cu_2O, CBTS, CdTe, V_2O_5, spiro-OMeTAD, CuI or P_3HT with optimized doping levels[11] and (3) contact optimization to minimize series resistance and improve charge extraction.[12]

4.2.2. Film quality control. Achieving the uniform, defect-free films assumed in our model requires: (1) controlled crystallization through anti-solvent engineering or thermal annealing[104] (2) grain boundary passivation strategies to reduce non-radiative recombination[105] and (3) thickness uniformity control, particularly critical for the thin absorber layers predicted to be optimal[106]

4.3. Comparison with experimental benchmarks

4.3.1. Similar architecture performance. While direct experimental data for $CsCdI_3$ devices is limited, comparison with related systems provides context:

Table 6 distinguishes the performance parameters of the six device configurations established in this study from those in previously published works. By combining ETL and HTL with $CsCdI_3$, Jabar *et al.* (2024) obtained a PCE of 19.03% when experimenting with the same absorber material ($CsCdI_3$).[34] In this comprehensive study, we conducted an in-depth analysis of six distinct photovoltaic architectural structures: ITO/PCBM/$CsCdI_3$/MoS_2/Ni, ITO/LBSO/$CsCdI_3$/MoS_2/Ni, ITO/SnS_2/$CsCdI_3$/MoS_2/Ni, ITO/IGZO/$CsCdI_3$/MoS_2/Ni, ITO/WS_2/$CsCdI_3$/MoS_2/Ni, and ITO/ZnO/$CsCdI_3$/MoS_2/Ni. The PCE values for these configurations were measured as 22.82%, 23.24%, 24.6%, 24.85%, 25.05%, and 25.06%, respectively, demonstrating a clear progression in efficiency across the different electron transport materials utilized. The V_{OC} values recorded were 0.9336, 0.9341, 0.9357, 0.9359, 0.9362, and 0.9362 V, showing incremental improvements with each configuration change. Similarly, the FF values were determined to be 87.01, 87.02, 87.12, 87.12, 87.14, and 87.14%, exhibiting subtle yet significant enhancements across the series. Upon careful examination and detailed analysis of the experimental results, we observed that the ZnO and WS2-based configurations yielded nearly identical V_{OC} and FF parameters, specifically 0.9362 V and 87.14%,

Table 6 PV parameters comparison with other published works of $CsCdI_3$-based PSC[a]

Type	Device structure	V_{OC} (V)	J_{SC} (mA cm^{-2})	FF (%)	PCE (%)	Ref.
E	FTO/TiO$_2$/CsPbI$_3$/spiro/Ag	0.66	11.92	52.47	4.13	107
E	FTO/TiO$_2$/CsPbI$_3$/spiro/Au	1.11	14.88	65	10.74	108
E	FTO/TiO$_2$/CsPbI$_3$/spiro/Ag	1.11	20.23	82	18.40	109
E	FTO/TiO$_2$/CsPbI$_3$/C	0.79	18.5	65	9.5	110
E	FTO/TiO$_2$/CsPbI$_3$/PTAA/Au	1.059	18.95	75.1	15.07	111
T	SnO$_x$/CsCdI$_3$/CdTe	0.9	55	76.5	19.03	34
T	ITO/PCBM/CsCdI$_3$/MoS$_2$/Ni	0.9336	28.09513	87.01	22.82	*
T	ITO/LBSO/CsCdI$_3$/MoS$_2$/Ni	0.9341	28.58713	87.02	23.24	*
T	ITO/SnS$_2$/CsCdI$_3$/MoS$_2$/Ni	0.9357	30.179453	87.12	24.6	*
T	ITO/IGZO/CsCdI$_3$/MoS$_2$/Ni	0.9359	30.471072	87.12	24.85	*
T	ITO/WS$_2$/CsCdI$_3$/MoS$_2$/Ni	0.9362	30.7086	87.14	25.05	*
T	ITO/ZnO/CsCdI$_3$/MoS$_2$/Ni	0.9362	30.71887	87.14	25.06	*

[a] E = experimental; T = theoretical; * = this work.

respectively. It was also noted that both the SnS_2 and IGZO-based architectural arrangements produced equivalent FF values of 87.12%. These findings represent a substantial improvement over previous experimental investigations that used $CsPbI_3$ as the primary absorber material and achieved PCE ranging from 4.13 to 18.4% as illustrated in Table 6. Based on Shockley–Queisser's thorough balancing considerations, a semiconductor band gap of 1.34 eV (928 nm) is necessary to achieve the maximum light-to-electric power conversion efficiency for AM 1.5G illumination, which is 33.16%.[92] And the SQ limit of J_{SC} is 35.82 mA cm^{-2}.[92] After a thorough evaluation of all photovoltaic parameters and performance metrics, we conclusively determined that the ITO/ZnO/CsCdI$_3$/MoS$_2$/Ni configuration demonstrated superior overall performance with the highest optimization of critical photovoltaic characteristics, making it the most promising candidate for future development and practical applications in solar cell technology.

4.3.2. Performance gap analysis. The discrepancy between our simulated results and typical experimental values for similar Cs-based perovskites can be attributed to: (1) defect density assumptions: our model assumes relatively low defect densities (10^{15}–10^{16} cm^{-3}), while experimental films often exhibit higher trap densities,[112] (2) interface recombination: simulations may underestimate interfacial recombination losses that dominate in real devices,[113] (3) optical losses: parasitic absorption in transport layers and reflection losses not fully captured in device modeling,[92] and (4) environmental stability: degradation mechanisms not accounted for in steady-state simulations but critical for experimental performance.[114]

4.4. Recommendations for experimental realization

4.4.1 Based on our computational insights and known synthesis challenges. (1) Precursor engineering: develop CdI_2–CsI precursor solutions with additives to control crystallization kinetics,[115] (2) atmosphere control: synthesis under an inert atmosphere to prevent oxidation of Cd^{2+},[116] (3) interface modification: surface passivation strategies using Lewis bases to reduce trap states,[117] and (4) encapsulation strategies: robust encapsulation is required due to moisture sensitivity predicted from our defect calculations.[118]

4.5. Experimental implementation limitations

The SCAPS-1D simulation environment employed in this study, while providing valuable insights into device physics and optimization pathways, inherently assumes ideal conditions that may not be readily achievable in experimental implementations. The simulation framework does not account for several real-world factors that significantly impact device performance, including grain boundary effects, interfacial defect states beyond the specified defect densities, hysteresis phenomena, and long-term stability issues under operational conditions. Additionally, the one-dimensional nature of SCAPS-1D simulations cannot capture lateral non-uniformities in film thickness, composition variations, and three-dimensional charge transport phenomena that are prevalent in solution-processed thin films. The assumed perfect interfaces between layers in the

simulation may not reflect the complex interfacial chemistry and potential interdiffusion that occurs during device fabrication, particularly at elevated processing temperatures. Furthermore, the simulation does not incorporate the effects of moisture, oxygen exposure, and other environmental factors that significantly influence perovskite device performance and stability. While these limitations do not diminish the value of the computational predictions for identifying optimal device architectures and material parameters, they highlight the importance of systematic experimental validation and the expected performance gaps between simulated and fabricated devices, particularly in the initial stages of material development and device optimization.

5. Conclusion

This investigation enhances CsCdI$_3$-based lead-free single perovskite solar cells to achieve maximum efficiency and J_{SC} when combined with nine BMCs, eight HTLs, and six ETLs. Initial testing of BMCs revealed nickel (Ni) as the preferred choice, offering maximum PCE while providing a more cost-effective alternative to Pd, Pt, and Se. Following the initial optimization, MoS$_2$ was chosen from eight distinct HTLs and paired with six ETLs to generate six unique configurations. After adjusting various parameters for each of these six configurations, the best absorber thickness found for all structures was 500 nm, with absorber thicknesses ranging from 400 to 1200 nm. ETL thickness optimization showed that 200 nm was ideal for SnS$_2$, whereas 50 nm was optimal for the remaining ETLs. Furthermore, research was conducted on various N_t, ultimately identifying 10^{15} cm^{-3} as the optimal defect density. Further analysis revealed that the device performance reached its peak when the R_s was minimized while the R_{sh} was maximized. When both resistance parameters were adjusted experimentally, the findings consistently showed a performance degradation as the operating temperature increased. The performance of the ZnO ETL-based structure remains superior to that of among other ETLs under series, shunt, and temperature variations of 0–6 Ω cm², 10^1–10^7 Ω cm², and 270–470 K, respectively. Generation, recombination rates, and Mott–Schottky analysis were explored, demonstrating maximum generation rates at ~0.85 μm and the maximum recombination rate at 0.34635 μm. The highest recombination was 3.65574 × 10^{22} cm³ s^{-1} in the ITO/ZnO/CsCdI$_3$/MoS$_2$/Ni structure. The QE and J–V characteristics indicate a superior response for the ZnO ETL-based PSC. Compared to the initial devices, the final optimized structures had higher generation rates, QE, and J–V. The optimized structures are ITO/PCBM/CsCdI$_3$/MoS$_2$/Ni, ITO/LBSO/CsCdI$_3$/MoS$_2$/Ni, ITO/SnS$_2$/CsCdI$_3$/MoS$_2$/Ni, ITO/IGZO/CsCdI$_3$/MoS$_2$/Ni, ITO/WS$_2$/CsCdI$_3$/MoS$_2$/Ni, and ITO/ZnO/CsCdI$_3$/MoS$_2$/Ni and their efficiencies were found as 22.82%, 23.24%, 24.6%, 24.85%, 25.05%, and 25.06% respectively. Among the six assessed structures, ITO/ZnO/CsCdI$_3$/MoS$_2$/Ni demonstrated the best performance, with a PCE of 33.94%, V_{OC} of 0.9362 V, J_{SC} of 30.71887 mA cm^{-2}, and FF of 87.14%. Its band alignment is responsible for its exceptional performance. The cubic structure verified utilizing the Goldschmidt tolerance

factor, the octahedral factor, and a newly proposed tolerance factor. These results demonstrate that lead-free single perovskite materials represent a promising alternative and may prove to be a practical choice for solar absorption layers in future photovoltaic applications.

Author contributions

Ashraful Mujahid: investigation, methodology, data curation, conceptualization, writing – original manuscript; Mohammad Yasin Hayat Khan: formal analysis, software, conceptualization, review – editing; Md Mayen Uddin: formal analysis, data curation, review – editing; Fahad Alhashmi Alamer: formal analysis, methodology, data curation, review – editing; O. Alsalmi: formal analysis, validation, review – editing; Md. Rasheduzzaman: formal analysis, validation, review – editing; Md. Zahid Hasan: formal analysis, validation, supervision, review – editing.

Conflicts of interest

There is no conflict to declare.

Data availability

Data will be made available on request.

Acknowledgements

References

1 M. H. K. Rubel, S. K. Mitro, M. K. Hossain, K. M. Hossain, M. M. Rahaman, J. Hossain, B. K. Mondal, A. Akter, M. F. Rahman, I. Ahmed and A. K. M. A. Islam, *Mater. Today Commun.*, 2022, **33**, 104302.

2 S. Saurabh, M. K. Hossain, S. Singh, S. K. Agnihotri and D. P. Samajdar, *RSC Adv.*, 2023, **13**, 9878–9891.

3 M. R. Islam, M. S. Islam, M. Y. Zamil, N. Ferdous, C. Stampfl, J. Park and M. K. Hossain, *J. Phys. Chem. Solids*, 2023, **176**, 111263.

4 M. Hasan Ali, A. T. M. Saiful Islam, M. D. Haque, M. Ferdous Rahman, M. Khalid Hossain, N. Sultana and A. Z. M. Touhidul Islam, *Mater. Today Commun.*, 2023, **34**, 105387.

5 A. O. M. Maka and J. M. Alabid, *Clean Energy*, 2022, **6**, 476–483.

6 C. M. Díaz-Acosta, A. Martínez-Luévanos, S. Estrada-Flores, L. F. Cano-Salazar, E. N. Aguilera-González and M. C. Ibarra-Alonso, *Materia*, 2022, **26**, e13116.

7 M. I. Hossain, W. Qarony, M. K. Hossain, M. K. Debnath, M. J. Uddin and Y. H. Tsang, *Appl. Nanosci.*, 2017, **7**, 489–497.

8 M. K. Basher, M. K. Hossain and M. A. R. Akand, *Optik*, 2019, **176**, 93–101.

9 H. Bencherif and M. K. Hossain, *Sol. Energy*, 2022, **248**, 137–148.

10 M. K. A. Mohammed, A. K. Al-Mousoi, S. Singh, A. Kumar, M. K. Hossain, S. Q. Salih, P. Sasikumar, R. Pandey, A. A. Yadav and Z. M. Yaseen, *Opt. Mater.*, 2023, **138**, 113702.

11 Y. Luo, G. Chen, S. Chen, N. Ahmad, M. Azam, Z. Zheng, Z. Su, M. Cathelinaud, H. Ma, Z. Chen, P. Fan, X. Zhang and G. Liang, *Adv. Funct. Mater.*, 2023, **33**, 2213941.

12 S. Heckeroth, The Promise of Thin-Film Solar, *Mother Earth News*, 2010.

13 M. K. Hossain, A. A. Arnab, R. C. Das, K. M. Hossain, M. H. K. Rubel, M. F. Rahman, H. Bencherif, M. E. Emetere, M. K. A. Mohammed and R. Pandey, *RSC Adv.*, 2022, **12**, 34850–34873.

14 M. K. Hossain, M. H. K. Rubel, G. F. I. Toki, I. Alam, M. F. Rahman and H. Bencherif, *ACS Omega*, 2022, **7**, 43210–43230.

15 K. Miyata, T. L. Atallah and X.-Y. Zhu, *Sci. Adv.*, 2017, **3**, e1701469.

16 A. Zeb, Z. Sun, T. Khan, M. A. Asghar, Z. Wu, L. Li, C. Ji and J. Luo, *Inorg. Chem. Front.*, 2017, **4**, 1485–1492.

17 A. Kojima, K. Teshima, Y. Shirai and T. Miyasaka, *J. Am. Chem. Soc.*, 2009, **131**, 6050–6051.

18 W.-J. Yin, J.-H. Yang, J. Kang, Y. Yan and S.-H. Wei, *J. Mater. Chem. A*, 2015, **3**, 8926–8942.

19 Z. Chen, J. Wang, Y. Ren, C. Yu and K. Shum, *Appl. Phys. Lett.*, 2012, **101**(9), DOI: **10.1063/1.4748888**.

20 M. K. Hossain, S. Bhattarai, A. A. Arnab, M. K. A. Mohammed, R. Pandey, M. H. Ali, M. F. Rahman, M. R. Islam, D. P. Samajdar, J. Madan, H. Bencherif, D. K. Dwivedi and M. Amami, *RSC Adv.*, 2023, **13**, 21044–21062.

21 E. Fransson, P. Rosander, F. Eriksson, J. M. Rahm, T. Tadano and P. Erhart, *Commun. Phys.*, 2023, **6**, 173.

22 Y. Doumbia, A. Bouich, B. M. Soucase and D. Soro, *JOM*, 2023, **75**, 4479–4484.

23 B. A. Rosales, L. Wei and J. Vela, *J. Solid State Chem.*, 2019, **271**, 206–215.

24 Q. Wu, X. Liu, S. Xu, H. Pi, X. Han, Y. Liu and Y. Li, *Dalton Trans.*, 2019, **48**, 6787–6793.

25 K. Hirose, K. Kawamura, Y. Ohishi, S. Tateno and N. Sata, *Am. Mineral.*, 2005, **90**, 262–265.

26 S. Tateno, K. Hirose, N. Sata and Y. Ohishi, *Phys. Chem. Miner.*, 2006, **32**, 721–725.

27 K. Hirose and Y. Fujita, *Geophys. Res. Lett.*, 2005, **32**, 2005GL023219.

28 B. Wang and K. Ohgushi, *Sci. Rep.*, 2016, **6**, 37896.

29 A. Jabar, S. Benyoussef and L. Bahmad, *Opt. Quantum Electron.*, 2023, **55**, 839.

30 A. Jabar, H. Labrim, L. Laanab, B. Jaber, L. Bahmad and S. Benyoussef, *Mod. Phys. Lett. B*, 2023, **37**, 2350132.

31 M. K. Hossain, D. P. Samajdar, R. C. Das, A. A. Arnab, M. F. Rahman, M. H. K. Rubel, M. R. Islam, H. Bencherif, R. Pandey, J. Madan and M. K. A. Mohammed, *Energy Fuels*, 2023, **37**, 3957–3979.

32 M. K. Hossain, M. K. A. Mohammed, R. Pandey, A. A. Arnab, M. H. K. Rubel, K. M. Hossain, M. H. Ali, M. F. Rahman,

H. Bencherif, J. Madan, M. R. Islam, D. P. Samajdar and S. Bhattarai, *Energy Fuels*, 2023, **37**, 6078–6098.

33 H. J. Snaith, *Nat. Mater.*, 2018, **17**, 372–376.

34 A. Jabar, S. Benyoussef and L. Bahmad, *Trans. Electr. Electron. Mater.*, 2024, **25**, 519–528.

35 M. A. Momin, M. R. Islam, M. A. Sarker, M. Solayman, R. K. Sharme, M. R. Islam and S. Ahmad, *Adv. Condens. Matter Phys.*, 2025, **2025**, 9968037.

36 T. Leijtens, G. E. Eperon, N. K. Noel, S. N. Habisreutinger, A. Petrozza and H. J. Snaith, *Adv. Energy Mater.*, 2015, **5**, 1500963.

37 W. Xu, X. Yao, T. Meng, K. Wang, F. Huang, X. Gong and Y. Cao, *J. Mater. Chem. C*, 2017, **5**, 4190–4197.

38 M. K. Hossain, M. T. Rahman, M. K. Basher, M. J. Afzal and M. S. Bashar, *Results Phys.*, 2018, **11**, 1172–1181.

39 M. K. Hossain, A. A. Mortuza, S. K. Sen, M. K. Basher, M. W. Ashraf, S. Tayyaba, M. N. H. Mia and M. J. Uddin, *Optik*, 2018, **171**, 507–516.

40 M. K. Hossain, M. F. Pervez, M. J. Uddin, S. Tayyaba, M. N. H. Mia, M. S. Bashar, M. K. H. Jewel, M. A. S. Haque, M. A. Hakim and M. A. Khan, *Mater. Sci.*, 2017, **36**, 93–101.

41 M. K. Hossain, M. F. Pervez, M. N. H. Mia, A. A. Mortuza, M. S. Rahaman, M. R. Karim, J. M. M. Islam, F. Ahmed and M. A. Khan, *Results Phys.*, 2017, **7**, 1516–1523.

42 S. Li, Y.-L. Cao, W.-H. Li and Z.-S. Bo, *Rare Met.*, 2021, **40**, 2712–2729.

43 F. M. Rombach, S. A. Haque and T. J. Macdonald, *Energy Environ. Sci.*, 2021, **14**, 5161–5190.

44 A. K Al-Mousoi, M. K. A. Mohammed, S. Q. Salih, R. Pandey, J. Madan, D. Dastan, E. Akman, A. A. Alsewari and Z. M. Yaseen, *Energy Fuels*, 2022, **36**, 14403–14410.

45 R. A. Jabr, M. Hamad and Y. Mohanna, *Int. J. Electr. Eng. Educ.*, 2007, **44**, 23–33.

46 Y. H. Khattak, Modeling of high power conversion efficiency thin film solar cells, PhD thesis, Universitat Politècnica de València, 2019.

47 M. K. Hossain, O. Alsalman, S. Rana, M. S. Uddin, G. F. I. Toki, S. H. Shahatha, M. R. Mohammad, M. A. Darwish, P. Sasikumar, S. Haq, H. Bencherif and R. Haldhar, *Inorg. Chem. Commun.*, 2024, **168**, 112964.

48 M. K. Hossain, M. A. Islam, M. S. Uddin, P. Paramasivam, J. A. Hamid, R. A. Alshgari, V. K. Mishra and R. Haldhar, *Sci. Rep.*, 2024, **14**, 30142.

49 M. K. Hossain, A. K. Datta, O. Alsalman, M. S. Uddin, G. F. I. Toki, M. A. Darwish, M. R. Mohammad, D. K. Dwivedi, R. Haldhar and S. V. Trukhanov, *Results Phys.*, 2024, **61**, 107751.

50 M. Y. Rahman and S. M. Mominuzzaman, *arXiv*, 2024, preprint, arXiv:2401.09584, DOI: 10.48550/arXiv.2401.09584.

51 M. H. Ishraq, M. Tarekuzzaman, J. K. Modak, S. Ahmad, M. Rasheduzzaman, Y. Arafat and M. Z. Hasan, *Mater. Sci. Eng., B*, 2024, **308**, 117622.

52 M. A. Bakkar Siddique, M. S. Parves, M. Tarekuzzaman, M. R. Kabir, M. S. M. Al-Saleem, J. Y. Al-Humaidi, M. Rasheduzzaman, M. M. Hossen, M. M. Rahman and M. Z. Hasan, *Langmuir*, 2025, **41**, 19797–19820.

53 M. K. Hossain, G. F. I. Toki, A. Kuddus, M. H. K. Rubel, M. M. Hossain, H. Bencherif, M. F. Rahman, M. R. Islam and M. Mushtaq, *Sci. Rep.*, 2023, **13**, 2521.

54 C. J. Bartel, C. Sutton, B. R. Goldsmith, R. Ouyang, C. B. Musgrave, L. M. Ghiringhelli and M. Scheffler, *Sci. Adv.*, 2019, **5**(2), eaav0693.

55 V. M. Goldschmidt, *Naturwissenschaften*, 1926, **14**, 477–485.

56 C. Li, X. Lu, W. Ding, L. Feng, Y. Gao and Z. Guo, *Acta Crystallogr., Sect. B: Struct. Sci.*, 2008, **64**, 702–707.

57 R. D. Shannon, *Acta Crystallogr., Sect. A*, 1976, **32**, 751–767.

58 N. Singh, A. Agarwal and M. Agarwal, *Sol. Energy*, 2020, **208**, 399–410.

59 H. B. Michaelson, *J. Appl. Phys.*, 1977, **48**, 4729–4733.

60 F. Behrouznejad, S. Shahbazi, N. Taghavinia, H.-P. Wu and E. W.-G. Diau, *J. Mater. Chem. A*, 2016, **4**, 13488–13498.

61 Band alignments of different buffer layers (CdS, Zn(O,S), and In2S3) on Cu2ZnSnS4 | Applied Physics Letters | AIP Publishing, https://pubs.aip.org/aip/apl/article-abstract/104/17/173901/24799/Band-alignments-of-different-buffer-layers-CdS-Zn?redirectedFrom=fulltext, (accessed August 6, 2025).

62 S. Abdelaziz, A. Zekry, A. Shaker and M. Abouelatta, *Opt. Mater.*, 2020, **101**, 109738.

63 A. A. Goje, N. A. Ludin, M. A. Mat Teridi, U. Syafiq, M. A. Ibrahim, F. Nawab and A. A. Syakirin, *IOP Conf. Ser.: Mater. Sci. Eng.*, 2023, **1278**, 012004.

64 M. K. Hossain, M. S. Uddin, G. F. I. Toki, M. K. A. Mohammed, R. Pandey, J. Madan, M. F. Rahman, M. R. Islam, S. Bhattarai, H. Bencherif, D. P. Samajdar, M. Amami and D. K. Dwivedi, *RSC Adv.*, 2023, **13**, 23514–23537.

65 M. Tripathi, V. Vaibhav, B. Sengar and A. Ullas, *Mater. Today: Proc.*, 2022, **62**, 4327–4331.

66 S. Rai, B. K. Pandey and D. K. Dwivedi, *Opt. Mater.*, 2020, **100**, 109631.

67 M. T. Islam, M. R. Jani, S. M. Al Amin, M. S. U. Sami, K. M. Shorowordi, M. I. Hossain, M. Devgun, S. Chowdhury, S. Banerje and S. Ahmed, *Opt. Mater.*, 2020, **105**, 109957.

68 I. Alam and M. A. Ashraf, *Energy Sources, Part A*, 2024, **46**, 17080–17096.

69 B. A. Al-Asbahi, S. M. H. Qaid, M. Hezam, I. Bedja, H. M. Ghaithan and A. S. Aldwayyan, *Opt. Mater.*, 2020, **103**, 109836.

70 A. F. Akbulatov, L. A. Frolova, S. A. Tsarev, I. Zhidkov, S. Yu. Luchkin, E. Z. Kurmaev, K. J. Stevenson, S. M. Aldoshin and P. A. Troshin, *J. Phys. Chem. C*, 2020, **124**, 21378–21385.

71 K. Sobayel, M. Akhtaruzzaman, K. S. Rahman, M. T. Ferdaous, Z. A. Al-Mutairi, H. F. Alharbi, N. H. Alharthi, M. R. Karim, S. Hasmady and N. Amin, *Results Phys.*, 2019, **12**, 1097–1103.

72 I. Montoya De Los Santos, H. J. Cortina-Marrero, M. A. Ruíz-Sánchez, L. Hechavarría-Difur, F. J. Sánchez-Rodríguez, M. Courel and H. Hu, *Sol. Energy*, 2020, **199**, 198–205.

73 N. Chawki, M. Rouchdi and B. Fares, Numerical study of BaZrS3 based chalcogenide perovskite solar cell using

SCAPS-1D device simulation, *Research Square*, 2022, preprint, DOI: 10.21203/rs.3.rs-1251663/v1.

74 N. J. Valeti, K. Prakash and M. K. Singha, *Results Opt.*, 2023, **12**, 100440.

75 I. Alam, R. Mollick and M. A. Ashraf, *Phys. B*, 2021, **618**, 413187.

76 A. Owolabi, M. Onimisi, J. Ukwenya, A. Bature, U. Ushiekpan and U. Ushiekpan, *Am. J. Phys. Appl.*, 2020, **8**, 8–18.

77 S. Karthick, S. Velumani and J. Bouclé, *Sol. Energy*, 2020, **205**, 349–357.

78 E. H. Jung, N. J. Jeon, E. Y. Park, C. S. Moon, T. J. Shin, T.-Y. Yang, J. H. Noh and J. Seo, *Nature*, 2019, **567**, 511–515.

79 E. Bi, W. Tang, H. Chen, Y. Wang, J. Barbaud, T. Wu, W. Kong, P. Tu, H. Zhu, X. Zeng, J. He, S. Kan, X. Yang, M. Grätzel and L. Han, *Joule*, 2019, **3**, 2748–2760.

80 D. Bogachuk, R. Tsuji, D. Martineau, S. Narbey, J. P. Herterich, L. Wagner, K. Suginuma, S. Ito and A. Hinsch, *Carbon*, 2021, **178**, 10–18.

81 K. Tvingstedt, L. Gil-Escrig, C. Momblona, P. Rieder, D. Kiermasch, M. Sessolo, A. Baumann, H. J. Bolink and V. Dyakonov, *ACS Energy Lett.*, 2017, **2**, 424–430.

82 Y. Li, B. Ding, Q.-Q. Chu, G.-J. Yang, M. Wang, C.-X. Li and C.-J. Li, *Sci. Rep.*, 2017, **7**, 46141.

83 M. K. Hossain, G. F. Ishraque Toki, D. P. Samajdar, M. H. K. Rubel, M. Mushtaq, M. R. Islam, M. F. Rahman, S. Bhattarai, H. Bencherif, M. K. A. Mohammed, R. Pandey and J. Madan, *Energy Fuels*, 2023, **37**, 7380–7400.

84 A. Sunny, S. Rahman, M. M. Khatun and S. R. A. Ahmed, *AIP Adv.*, 2021, **11**, 065102.

85 Z. Ma, Z. Shi, C. Qin, M. Cui, D. Yang, X. Wang, L. Wang, X. Ji, X. Chen, J. Sun, D. Wu, Y. Zhang, X. J. Li, L. Zhang and C. Shan, *ACS Nano*, 2020, **14**, 4475–4486.

86 Y. Li, Z. Shi, L. Lei, F. Zhang, Z. Ma, D. Wu, T. Xu, Y. Tian, Y. Zhang, G. Du, C. Shan and X. Li, *Chem. Mater.*, 2018, **30**, 6744–6755.

87 S. R. Raga, E. M. Barea and F. Fabregat-Santiago, *J. Phys. Chem. Lett.*, 2012, **3**, 1629–1634.

88 M. Fischer, K. Tvingstedt, A. Baumann and V. Dyakonov, *ACS Appl. Energy Mater.*, 2018, **1**, 5129–5134.

89 G. G. Malliaras, J. R. Salem, P. J. Brock and C. Scott, *Phys. Rev. B: Condens. Matter Mater. Phys.*, 1998, **58**, R13411–R13414.

90 U. Mandadapu, V. Vedanayakam, K. Thyagarajan, M. Raja reddy and B. Babu, *Int. J. Renew. Energy Res.*, 2017, **7**, 1603–1612.

91 M. Samiul Islam, K. Sobayel, A. Al-Kahtani, M. A. Islam, G. Muhammad, N. Amin, M. Shahiduzzaman and M. Akhtaruzzaman, *Nanomaterials*, 2021, **11**, 1218.

92 S. Rühle, *Sol. Energy*, 2016, **130**, 139–147.

93 M. Liu, M. B. Johnston and H. J. Snaith, *Nature*, 2013, **501**, 395–398.

94 M. M. A. Moon, M. H. Ali, M. F. Rahman, A. Kuddus, J. Hossain and A. B. M. Ismail, *Phys. Scr.*, 2020, **95**, 035506.

95 M. F. Rahman, M. J. A. Habib, M. H. Ali, M. H. K. Rubel, M. R. Islam, A. B. M. Ismail and M. K. Hossain, *AIP Adv.*, 2022, **12**, 105317.

96 K. R. McIntosh, D. Yan, K. C. Fong and T. C. Kho, *J. Appl. Phys.*, 2014, **116**(6), DOI: 10.1063/1.4893176.

97 K. Sekar, L. Marasamy, S. Mayarambakam, H. Hawashin, M. Nour and J. Bouclé, *RSC Adv.*, 2023, **13**, 25483–25496.

98 E. von Hauff and D. Klotz, *J. Mater. Chem. C*, 2022, **10**, 742–761.

99 A. Guerrero, J. Bisquert and G. Garcia-Belmonte, *Chem. Rev.*, 2021, **121**, 14430–14484.

100 J.-C. Hebig, I. Kühn, J. Flohre and T. Kirchartz, *ACS Energy Lett.*, 2016, **1**, 309–314.

101 M. Leng, Y. Yang, K. Zeng, Z. Chen, Z. Tan, S. Li, J. Li, B. Xu, D. Li, M. P. Hautzinger, Y. Fu, T. Zhai, L. Xu, G. Niu, S. Jin and J. Tang, *Adv. Funct. Mater.*, 2018, **28**, 1704446.

102 L. Protesescu, S. Yakunin, M. I. Bodnarchuk, F. Krieg, R. Caputo, C. H. Hendon, R. X. Yang, A. Walsh and M. V. Kovalenko, *Nano Lett.*, 2015, **15**, 3692–3696.

103 A. Babayigit, A. Ethirajan, M. Muller and B. Conings, *Nat. Mater.*, 2016, **15**, 247–251.

104 N. J. Jeon, J. H. Noh, Y. C. Kim, W. S. Yang, S. Ryu and S. I. Seok, *Nat. Mater.*, 2014, **13**, 897–903.

105 S. Yang, S. Chen, E. Mosconi, Y. Fang, X. Xiao, C. Wang, Y. Zhou, Z. Yu, J. Zhao, Y. Gao, F. De Angelis and J. Huang, *Science*, 2019, **365**, 473–478.

106 G. E. Eperon, S. N. Habisreutinger, T. Leijtens, B. J. Bruijnaers, J. J. van Franeker, D. W. deQuilettes, S. Pathak, R. J. Sutton, G. Grancini, D. S. Ginger, R. A. J. Janssen, A. Petrozza and H. J. Snaith, *ACS Nano*, 2015, **9**, 9380–9393.

107 P. Luo, W. Xia, S. Zhou, L. Sun, J. Cheng, C. Xu and Y. Lu, *J. Phys. Chem. Lett.*, 2016, **7**, 3603–3608.

108 B. Li, Y. Zhang, L. Fu, T. Yu, S. Zhou, L. Zhang and L. Yin, *Nat. Commun.*, 2018, **9**, 1076.

109 Y. Wang, X. Liu, T. Zhang, X. Wang, M. Kan, J. Shi and Y. Zhao, *Angew. Chem.*, 2019, **131**, 16844–16849.

110 S. Xiang, Z. Fu, W. Li, Y. Wei, J. Liu, H. Liu, L. Zhu, R. Zhang and H. Chen, *ACS Energy Lett.*, 2018, **3**, 1824–1831.

111 K. Wang, Z. Jin, L. Liang, H. Bian, D. Bai, H. Wang, J. Zhang, Q. Wang and S. Liu, *Nat. Commun.*, 2018, **9**, 4544.

112 T. S. Sherkar, C. Momblona, L. Gil-Escrig, J. Ávila, M. Sessolo, H. J. Bolink and L. J. A. Koster, *ACS Energy Lett.*, 2017, **2**, 1214–1222.

113 P. Caprioglio, M. Stolterfoht, C. M. Wolff, T. Unold, B. Rech, S. Albrecht and D. Neher, *Adv. Energy Mater.*, 2019, **9**, 1901631.

114 C. C. Boyd, R. Cheacharoen, T. Leijtens and M. D. McGehee, *Chem. Rev.*, 2019, **119**, 3418–3451.

115 J.-W. Lee, H.-S. Kim and N.-G. Park, *Acc. Chem. Res.*, 2016, **49**, 311–319.

116 Z. Li, M. Yang, J.-S. Park, S.-H. Wei, J. J. Berry and K. Zhu, *Chem. Mater.*, 2016, **28**, 284–292.

117 N. De Marco, H. Zhou, Q. Chen, P. Sun, Z. Liu, L. Meng, E.-P. Yao, Y. Liu, A. Schiffer and Y. Yang, *Nano Lett.*, 2016, **16**, 1009–1016.

118 J. A. Christians, P. A. Miranda Herrera and P. V. Kamat, *J. Am. Chem. Soc.*, 2015, **137**, 1530–1538.